PERGAMON

Journal of Structural Geology 24 (2002) 1389–1411

JOURNAL OF STRUCTURAL GEOLOGY

www.elsevier.com/locate/jstrugeo

Displacement–length scaling in three dimensions: the importance of aspect ratio and application to deformation bands

Richard A. Schultz[a,*], Haakon Fossen[b]

[a]*Geomechanics–Rock Fracture Group, Department of Geological Sciences/172, Mackay School of Mines, University of Nevada, Reno, NV 89557, USA*
[b]*Department of Geology, University of Bergen, Allegaten 41, N-5007 Bergen, Norway*

Received 17 November 2000; revised 18 July 2001; accepted 20 August 2001

Abstract

Deformation bands confined to a 9-m-thick layer of the Entrada Sandstone in Utah accumulate less displacement per unit length than fractures that are not stratigraphically confined. This difference in displacement–length (D–L) scaling is related to the increasing length-to-height (aspect) ratio of the bands. Here we derive new expressions for displacement–length scaling and fracture strain for three-dimensional (3-D) elliptical fractures. The maximum (relative) displacement D_{max} on an elliptical fracture surface depends on the fracture geometry (both length L and height H), the end-zone length (through driving stress and the rock's yield strength), and the properties of the surrounding rock (modulus, Poisson's ratio). A given elliptical fracture will show different values of D_{max}/L in horizontal and vertical sections due to differences in fracture dimension (length vs. height) and end-zone length. A population of elliptical fractures can accommodate less displacement or strain if fracture aspect ratios increase with L than a population of fractures having constant aspect ratios. These relationships reveal how 3-D fracture geometries systematically influence the population statistics. The magnitude of horizontal (extensional) fracture strain accommodated by the population of deformation bands predicted by the analysis is consistent with that obtained independently from traverse measurements on the outcrop (0.12%). The 3-D fracture geometry can contribute at least an order of magnitude in displacement deficit (or excess) relative to tall 2-D fractures and comparable scatter on maximum displacement vs. length (D–L) diagrams. In general, fractures confined to stratigraphic layers grow nonproportionally ($L/H \neq$ constant for $L >$ the layer thickness), leading to reduced capacity to accommodate displacement and a shallower slope on the D–L diagram. Similarly, fractures that grow by segment linkage (preferentially down-dip or along-strike) scale as nonproportional 3-D fractures. A unit slope on D–L diagrams implies proportional growth ($L/H =$ constant). Faults with slip surfaces and other fractures with nonpreferred growth directions can produce unit slopes, so that particular trajectories on D–L diagrams can reveal physical controls on fracture growth, such as stratigraphic confinement or segment interaction and linkage. © 2002 Published by Elsevier Science Ltd.

Keywords: Displacement–length scaling; Deformation bands; Fault growth; Fracture populations; Structural geology

1. Introduction and background

Displacement-length (D–L) scaling of fractures is understood by using two-dimensional (2-D) fracture mechanics models (e.g. Cowie and Scholz, 1992b) that assume plane conditions (e.g. Irwin, 1962; Heald et al., 1972; Palmer and Rice, 1972; Rudnicki, 1980; Kanninen and Popelar, 1985, pp. 69, 153; Bürgmann et al., 1994). In rock mechanics, a 2-D analysis idealizes a volume with fractures as a rectangular plate in an xy (Cartesian) coordinate system, with the vertical (z, 'thickness') dimension included only implicitly (Timoshenko and Goodier, 1970, pp. 15–17; Tada et al., 2000, pp. 14–15). The thickness of a 'thin' (plane stress) 2-D plate is negligible compared with the in-plane (xy) dimensions, so that in-plane stresses (σ_{xx}, σ_{yy}, σ_{xy}) can produce warping and strain of the plate in the out-of-plane (z) direction. In contrast, the thickness of a 'thick' (plane strain) plate is sufficiently large to prevent strain in the out-of-plane (z) direction in response to the in-plane stresses. A fracture in a 2-D analysis is oriented perpendicular to the in-plane directions so that variations in stress or displacement in the z-direction are not introduced (e.g. Paris and Sih, 1965; Anderson, 1995, pp. 23, 36, 56). Looking down the thickness (z) direction onto the surface of the plate, the planar fracture is represented as a line of length L within the xy coordinate system. Because the vertical (third, z) dimension is not considered explicitly in a 2-D stress analysis, neither is the fracture's height (its dimension in the z-direction, H). In that 2-D analysis, the length and displacement are associated (Fig. 1) without directly

* Corresponding author. Tel.: +1-775-784-4318; fax: +1-775-784-1833.
E-mail addresses: schultz@mines.unr.edu (R.A. Schultz), haakon.fossen@geol.uib.no (H. Fossen).

0191-8141/02/$ - see front matter © 2002 Published by Elsevier Science Ltd.
PII: S0191-8141(01)00146-8

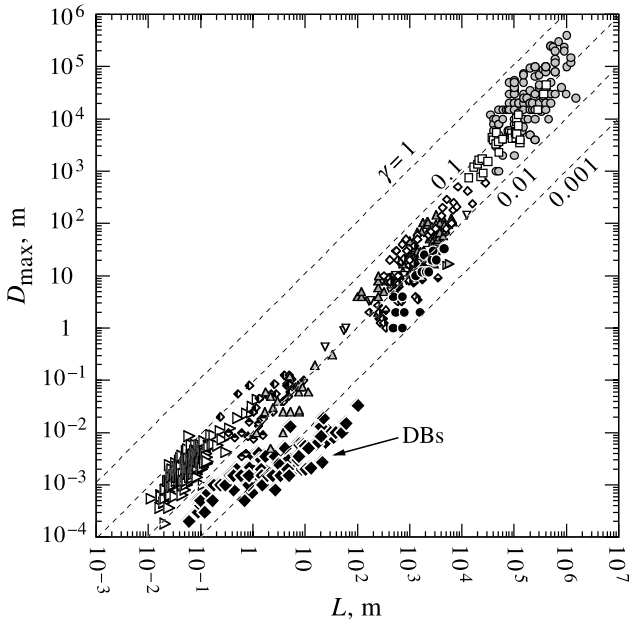

Fig. 1. Compilation of displacement–length data displayed on a traditional 2-D diagram. Deformation band ('DB') data from Fossen and Hesthammer (1997; 'DBs' in the figure); fault data are from Cowie and Scholz (1992a, and references therein), Gudmundsson and Bäckström (1991), Dawers et al. (1993), Cartwright et al. (1995), Schlische et al. (1996) and Krantz (1988). Dashed lines show contours of approximate 2-D fracture shear strain $\gamma = D_{max}/L$.

considering the influence of fracture height, leading to the standard D–L scaling relations that only incorporate displacement and length (e.g. Muraoka and Kamata, 1983; Cowie and Scholz, 1992a,b; Clark and Cox, 1996; Fossen and Hesthammer, 1997; Renshaw, 1997; Gudmundsson, 2000; Bonnet et al., 2001).

In contrast, a 3-D stress analysis of a fractured rock mass explicitly considers dimensions, stresses, and displacements in all three (*xyz*) directions, including the fracture's height and shape. As noted by Segall and Pollard (1980), Scholz (1982), Olson (1993), Nicol et al. (1996), Willemse (1997), Martel and Boger (1998), Kattenhorn et al. (2000), Schultz (2000), and others, fracture heights can be much smaller than (or comparable with) their lengths, leading to different D–L scaling relations (Willemse et al., 1996). Indeed, several studies have shown that the shorter dimension controls the displacement magnitude and associated fracture interaction distance (Segall and Pollard, 1980; Pollard and Segall, 1987; Olson, 1993; Pollard et al., 1993; Willemse, 1997; Cowie, 1998; Crider and Pollard, 1998; Gudmundsson, 2000).

A 3-D fracture is defined in this paper as an elliptical surface with specified values of length, height, dip, and maximum relative displacement in a 3-D *xyz* coordinate system (e.g. Irwin, 1962; Kassir and Sih, 1966; Willemse, 1997; see Tada et al. (2000, pp. 14–15)) for terminology particular to the small region near the fracture tip). Physically, the maximum relative displacement (D_{max}) on a fracture depends explicitly on both length L and height H (e.g. Irwin, 1962; Kassir and Sih, 1966; Chell, 1977; Willemse et al., 1996; Willemse, 1997; Martel and Boger, 1998), implying that the D–L scaling relations may differ for a 3-D fracture from those that ignore fracture height (the 2-D plane approach discussed above). An explicit consideration of the elliptical shapes of natural (3-D) fracture surfaces can be critically important for understanding the stresses and displacements in the vicinity of the fracture (e.g. Olson, 1993; Willemse, 1997; Crider and Pollard, 1998; Kattenhorn et al., 2000), and by implication, the balance between displacement accumulation and propagation of the fracture's tipline (Rubin, 1992; Willemse and Pollard, 2000). We demonstrate in this paper how the D–L scaling relations depend on both dimensions (length and height) of the fracture plane.

Deformation bands from the Jurassic Entrada Sandstone of southeastern Utah accumulate less displacement per unit length than do well-developed faults (Fossen and Hesthammer, 1997, 1998). These cataclastic deformation bands (Aydin, 1978b; Aydin and Johnson, 1978; Davis, 1999; Fossen, 2000) are confined to a 9-m-thick (Aydin, 1978a) porous sandstone layer within the Entrada Sandstone (Fig. 2) and also lack slip surfaces (Fossen and Hesthammer, 1998); deformation bands that accommodate larger, discontinuous displacements (of more than several meters) along corrugated slickensided slip surfaces transect the Entrada Sandstone (Aydin, 1978b; Fig. 2c). The deformation bands that lack slip surfaces scale according to $D_{max} = \gamma L^{0.5}$ (Fossen and Hesthammer, 1997), whereas other fault sets scale with an exponent closer to 1.0 (e.g. Cowie and Scholz, 1992a; Clark and Cox, 1996). Fossen and Hesthammer (1997, 1998) hypothesized that the smaller exponent ($\sim$0.5) for the deformation bands could be attributed to a lesser degree of strain localization, with the exponent increasing to 1.0 as they evolve into surfaces of discontinuous displacement.

In this paper we derive displacement–length scaling relations for elliptical fractures and apply them to stratigraphically confined deformation bands. We show that the maximum relative displacement (D_{max}) along a fracture is a continuous, explicit function of both its length and height, similar to the dependence of stress magnitude near an elliptical cavity given by the well-known Inglis/Kolosov relation (e.g. Timoshenko and Goodier, 1970, pp. 191–194; Rekash, 1979, pp. 134–138). We then explore the characteristics of this 3-D scaling relation on standard displacement–length diagrams and demonstrate that lines of constant 1.0 slope (with the associated values of fracture shear strain γ) are a special case of 3-D scaling in which aspect ratios remain constant throughout the population. The results reveal that the shallower (0.5) slope obtained from deformation bands reported by Fossen and Hesthammer (1997) is related to their 3-D geometry, and we discuss the implications of 3-D D–L scaling for fracture growth within stratigraphic layers and by segment linkage.

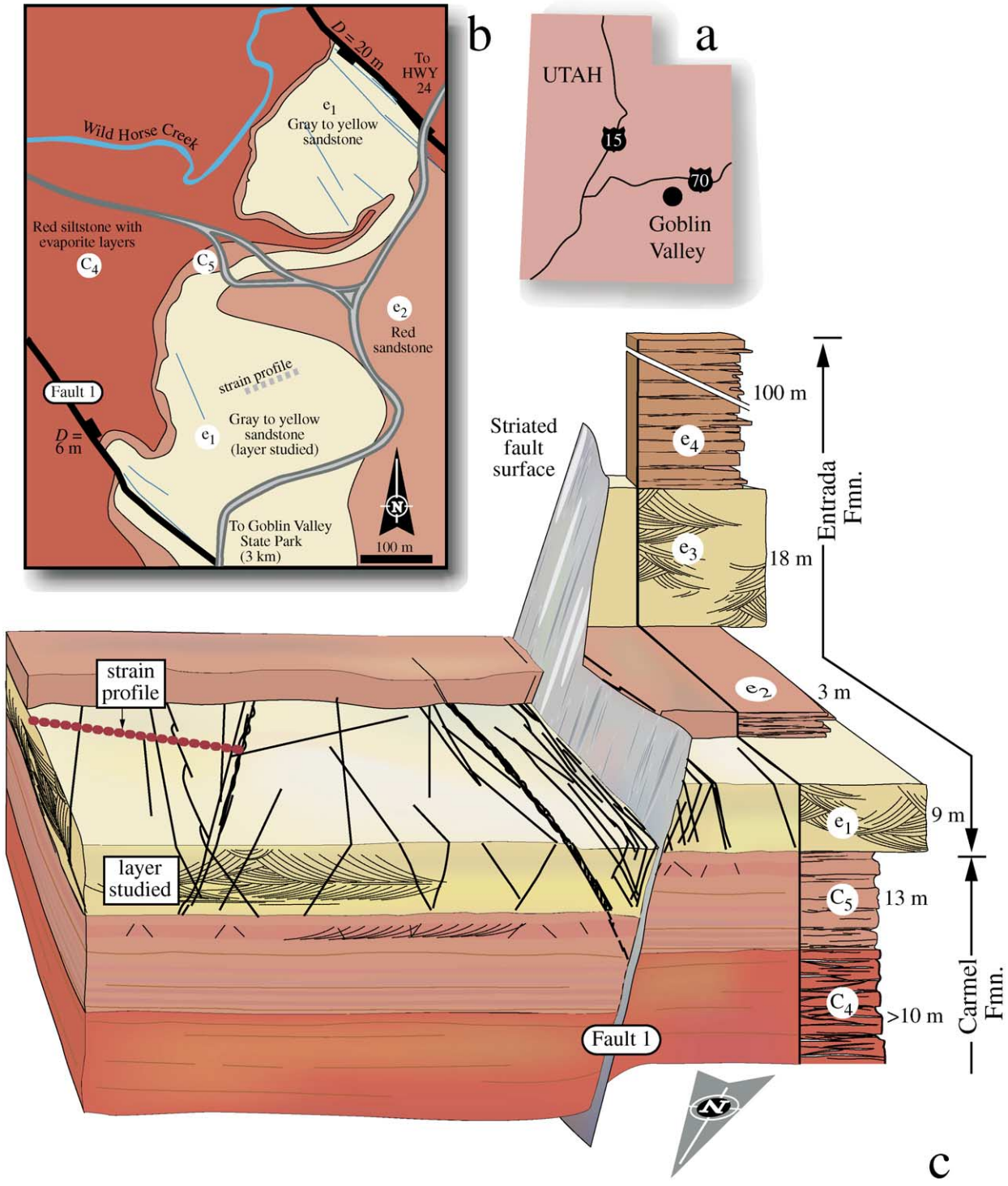

Fig. 2. (a) Map showing location of study area in Goblin Valley. (b) Simplified geologic map showing location of yellow-gray porous sandstone layer (e_1) and strain traverse (dotted line) in relation to faulted deformation bands (heavy lines with symbol on hanging wall). (c) Block diagram showing stratigraphy of study area and outcrop patterns of deformation bands (dipping lines in layer e_1).

2. The 3-D deformation band data set

Deformation bands in the Entrada Sandstone are narrow tabular zones of localized compactional and shearing displacement in an otherwise homogeneous stratigraphic layer (Aydin, 1978b; Fossen and Hesthammer, 1997; Davis, 1999). Recent work demonstrates that displacement distributions along deformation bands vary systematically with position (Antonellini and Aydin, 1995; Fossen and Hesthammer, 1997, 1998; Wibberley et al., 2000), similar

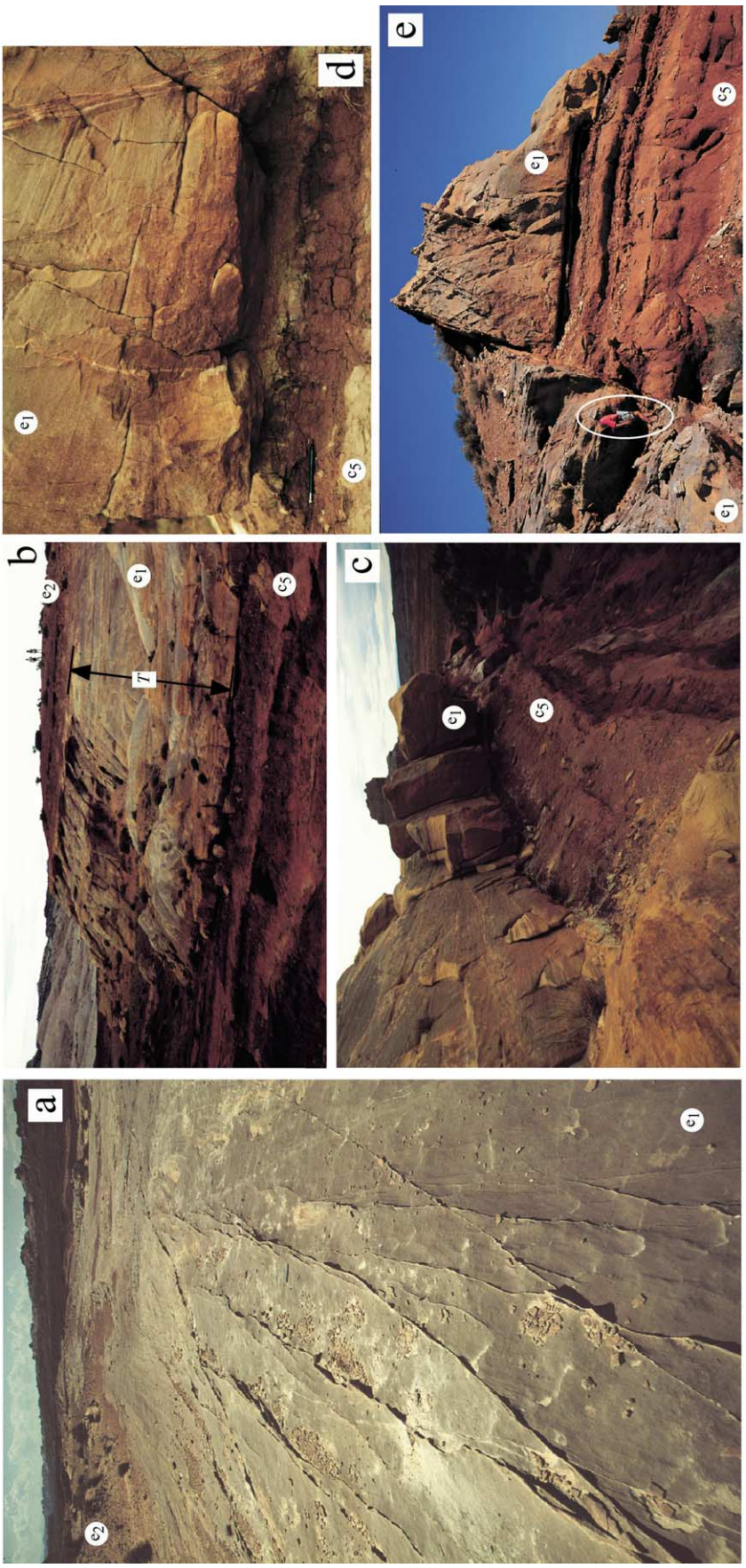

Fig. 3. (a) Deformation bands exposed as narrow ridges in subhorizontal outcrop of the porous yellow-gray sandy layer e_1 in Entrada Sandstone. (b) Cross-sectional view of layer e_1 showing 9 m thickness, T, subvertical bands, and reddish silty layers (e_2 and c_5 in Fig. 2c) above and below. Note graduate students on skyline for scale. (c) View along lower contact of layer e_1 with Carmel Formation (layer c_5) showing deformation bands (subvertical surfaces between blocks) terminating against underlying layer c_5. (d) Detail of lower contact of layer e_1 showing deformation bands decreasing in width toward c_5; note pencil for scale. (e) Normal fault in Entrada Sandstone ('Fault 1' in Fig. 2b and c) with corrugated slip surface and 6 m of dip-slip offset. Note offset of layers e_1 and c_5 (upper right of image) down on the left of the slip surface that truncates the network of deformation bands in its hanging wall, the high frequency of deformation bands visible in layer e_1, and the absence of deformation bands in the underlying layers. Geologist (circled) on hanging wall for scale.

to those of other fracture types (e.g. Muraoka and Kamata, 1983; Walsh and Watterson, 1988; Bürgmann et al., 1994; Gupta and Scholz, 2000). Displacement maxima occur far from band terminations where near-tip displacement gradients and band geometries (in outcrop) are consistent with mechanical interaction and band linkage (Cruikshank et al., 1991; Antonellini and Aydin, 1995; Fossen and Hesthammer, 1997; Willemse, 1997). Propagation of deformation bands appears related to stress changes induced near their terminations (e.g. Du and Aydin, 1993; Antonellini and Pollard, 1995) that, in turn, scale with the magnitude of displacements accommodated across them. Although the spacing between cataclastic deformation bands may be related to strain hardening within the bands and the remote strain distribution and magnitudes imposed on them (e.g. Antonellini et al., 1994), their lengths are related to their displacement distributions (Fossen and Hesthammer, 1997, 1998).

Nucleation and growth of deformation bands in sandstones are sensitive initially to porosity, grain size and sorting, presence of clay minerals, confining pressure, and differential stress and, with ongoing deformation, to the changes in these characteristics (e.g. Aydin and Johnson, 1983; Antonellini et al., 1994; Menéndez et al., 1996; Mair et al., 2000; Olsson, 2000; Bésuelle, 2001; Issen and Rudnicki, 2001). Observations of deformation bands in the field demonstrate that they can be confined to particular stratigraphic layers, for which band localization is facilitated, with growth across stratigraphic contacts inhibited where they encounter layers having unfavorable conditions (e.g. Fossen, 2000). Confinement of deformation bands to particular layers (e.g. Fig. 2a) is similar to joints, stylolites, and other types of localized strain that are also highly dependent on local stress state and lithologic properties for their development. As stratabound fractures lengthen, their aspect ratios increase, whereas their heights remain fixed by the stratigraphic thickness.

The deformation bands considered in this paper are confined to a well sorted and highly porous (i.e. ~20%) eolian yellow-gray layer within the Entrada Sandstone (Figs. 2 and 3a). The layer ('e_1' in Fig. 2c) is 9 m thick (Aydin, 1978a; and verified by us in the field in May 2001) and is bounded above and below by red silty sandstone layers that lack well-developed deformation bands ('e_2' and 'c_5' in Figs. 2c and 3b). Close examination of the contact regions reveals that the deformation bands within the yellow-gray layer consistently terminate at or just beyond the contacts with the red silty sandstone layers (Fig. 3c and d). The deformation bands span a range of lengths ($0.06 < L < 104$ m; Fossen and Hesthammer, 1997) but are confined to the yellow-gray layer (e_1), requiring that their heights be no more than the layer thickness, or $H \leq 9$ m. As a result, the three-dimensional shapes (length vs. height) of the bands scale with their lengths, with bands longer than 9 m becoming progressively less tall in relation to their lengths (Fig. 4c). The aspect (length/height) ratios of the deformation bands in the study area are largest for the longest bands ($L/H = 104/9$ m $= 11.6$), giving the bands a range of three-dimensional elliptical shapes. Faulted deformation bands that accommodate much larger displacements than those investigated in this paper (i.e. meters) are characterized by discontinuous displacement across their corrugated and slickensided surfaces (e.g. Aydin and Johnson, 1978; Fossen and Hesthammer, 1997; Shipton and Cowie, 2001). These faulted bands cut across

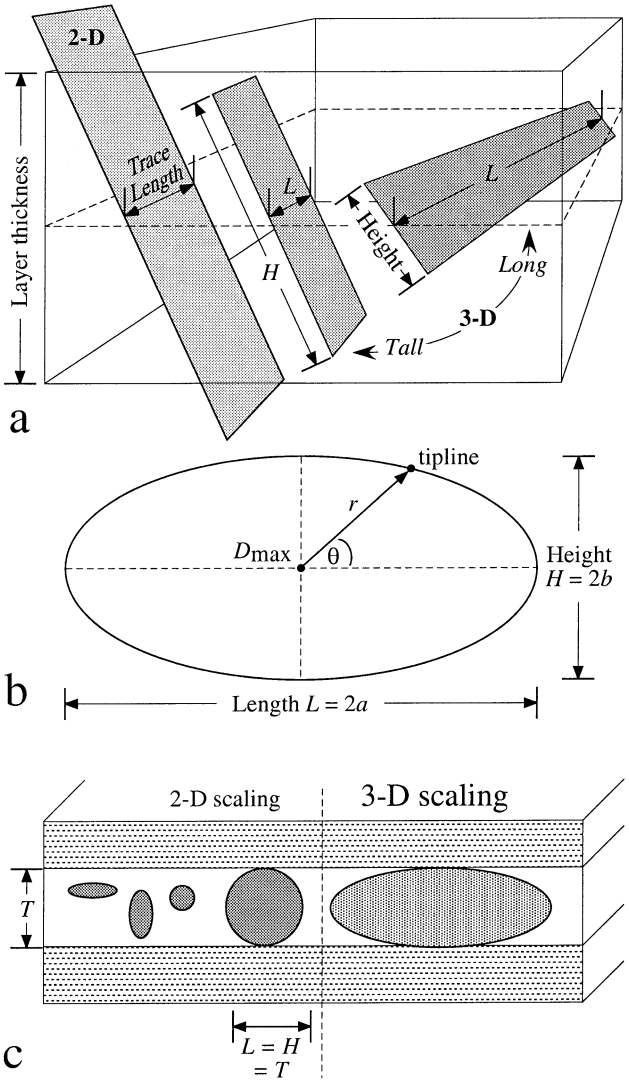

Fig. 4. (a) Geometry of dipping fracture planes within a layer. 3-D planar surfaces have measurable horizontal (trace) lengths and heights (measured in their planes); 2-D surfaces only provide measurements of their lengths. (b) Geometric parameters for an elliptical fracture in 3-D, with trace length L being twice the semi-horizontal axis ($L = 2a$) and height H being twice the semi-vertical axis ($H = 2b$) of the dipping plane. A fracture having its height much greater than its length ($2b \gg 2a$) is a 'tall' or 'tunnel' fracture that penetrates deeply into the rock mass relative to its length. A circular, equidimensional fracture ($2a = 2b$) is referred to as a 'penny' fracture. A 'long' fracture has $2a \gg 2b$. For a 2-D plane fracture, height ($2b$) is indefinitely large. (c) Diagram showing how fractures larger than the layer thickness T can grow only in length at constant height, leading to nonproportional growth and 3-D scaling.

stratigraphic contacts in the study area (e.g. Krantz, 1988; Fossen, 2000, p. 32; Figs. 2c and 3e).

3. Maximum displacement vs. fracture aspect ratio

We idealize a fracture as a degenerate (flat) ellipse having length $L = 2a$, height $H = 2b$, and a (much smaller) magnitude of relative displacement, with the maximum value of the relative-displacement distribution given by D_{max} (Fig. 4). A deformation band is modeled as an elliptical fracture. *Length* is defined in this paper as the horizontal trace (or map) length (Fig. 4a), whereas *height* is taken to be the vertical (i.e. down-dip) dimension of the fracture surface in its plane (cf. Watterson, 1986; Walsh and Watterson, 1988), following standard practice (e.g. Cowie and Scholz, 1992a,b; Dawers et al., 1993; Cartwright et al., 1995; Willemse et al., 1996; Gudmundsson, 2000). We apply results from elasticity theory and post-yield Elastic–Plastic Fracture Mechanics (EPFM) to construct an equation that explicitly relates D_{max}, length, and height, and we allow the length of the end zone (s) to vary as a free parameter, rather than being prescribed up-front as a constant (e.g. Cowie and Scholz, 1992b; Martel and Boger, 1998).

3.1. Elliptical (elastic) fracture shape

The stresses and displacements associated with an elliptical fracture in an infinite homogeneous elastic material are well known from Linear Elastic Fracture Mechanics (LEFM; e.g. Green and Sneddon, 1950; Irwin, 1962; Kassir and Sih, 1966; Xue and Qu, 1999; Zhu et al., 2001). The maximum (relative) displacement D_{max} on the LEFM fracture surface is given by:

$$D_{max} = \left[\frac{2(1-\nu)}{G}\sigma_d\right]\left(\frac{b}{E(a,b)}\right) \quad (1)$$

in which σ_d is the driving stress acting on the fracture (see Table 1), ν is Poisson's ratio, G is the shear modulus (both of the host rock), and a and b are the semi-major and semi-minor axes of the fracture (Fig. 4b), respectively. Driving stress is defined as the net traction (thought of as acting on the fracture) that leads to relative displacement of fracture

Table 1
Driving and resisting stresses for geologic fractures

Term	Symbol	Fracture type	Description	Source
Resolved stress on fracture[a]	S	Crack	Compressive normal stress	Rubin (1993)
	σ_a	Fault	State frictional strength	Cowie and Scholz (1992b)
	S_r	”	State frictional strength	Bürgmann et al. (1994)
	σ_r	DB[b]	Resolved remote stresses	This paper
	σ	Crack	Resolved tensile stress	Bilby et al. (1963); Chell (1977)
Internal ‘strength’ b.c.[c]	P_i	”	Internal fluid pressure	Rubin (1993)
	σ_f	Fault	Residual frictional strength	Cowie and Scholz (1992b)
	S_m	”	Strength of slipping patch	Bürgmann et al. (1994)
	τ_f	”	Resistive (residual) frictional stress	Rudnicki (1980); Cooke (1997)
	σ_i	DB	Mixed-mode grain-network strength	This paper
Driving stress	$(S - P_i)$	Crack	Effective tension	Rubin (1993)
	$(\sigma_a - \sigma_f)$	Fault	—	Cowie and Scholz (1992b)
	$(S_r - S_m)$	”	Stress drop	Bürgmann et al. (1994)
	σ_1	Crack	Remote (resolved) tension	Heald et al. (1972); Chell (1977)
	$(\sigma_r - \sigma_i)$	DB	Excess over grain-network strength	This paper
End zone constraint	σ_c	Crack	Cohesive stress	Rubin (1993)
	T_0	”	Modulus of cohesion, intrinsic toughness	Barenblatt (1962); Lawn (1993)
	σ_0	Fault	Shear strength of surrounding rock	Cowie and Scholz (1992b)
	S_c	”	Peak strength of end zone	Bürgmann et al. (1994)
	σ_p	DB	Peak strength of end zone	This paper
	$(\sigma_d - \sigma_y)$	”	Resisting stress in end zone	This paper
Yield strength	$(\sigma_c - P_i)$	Crack	Effective cohesive strength	Rubin (1993)
	$(\sigma_0 - \sigma_f)$	Fault	—	Cowie and Scholz (1992b)
	$(S_m - S_c)$	”	—	Bürgmann et al. (1994)
	$(\sigma_p - \sigma_i)$	DB	Yield strength of end zone	This paper

[a] Remote stresses resolved trigonometrically onto potential fracture plane; values applicable before fracture deforms and accommodates relative displacements.
[b] DB: deformation band.
[c] b.c.: boundary condition.

walls and concomitant amplification of stresses along the fracture's tip (in 2-D) or elliptical tipline (in 3-D). For joints and dikes (Table 1), σ_d is the resolved remote normal stress component (usually compressive) minus the internal pore-fluid pressure within the fracture (Pollard and Aydin, 1988; Rubin, 1993). For faults, σ_d is the maximum (static) frictional strength minus the residual frictional strength of the surface (Palmer and Rice, 1972; Rudnicki, 1980; Cooke, 1997). For deformation bands, the driving stress is related to the remote compressive and shear stress components resolved onto the band and the resistance of the band to compaction (Das, 1983, p. 36), cataclasis, and localized shearing σ_i (Table 1).

$E(a,b)$ in Eq. (1) is the complete elliptic integral of the second kind (e.g. Irwin, 1962; Kanninen and Popelar, 1985, p. 153; Lawn, 1993, p. 33), which is given by:

$$E(a,b) = \int_0^{\pi/2} \sqrt{1 - \left(\frac{a^2 - b^2}{a^2}\right)^2 \sin^2\varphi}\, d\varphi \qquad (2)$$

where φ is amplitude of the elliptic integral (Boas, 1966, pp. 410–413). Particular values of Eq. (2) can be obtained by specifying a and b and using standard mathematical tables to evaluate the integral (e.g. Beyer, 1987). For a circular, 'penny-shaped' fracture ($a = b$), $E(a,b) = \pi/2$, whereas a long, 2-D fracture ($a \gg b$) yields $E(a,b) = 1$ (see also Gudmundsson, 2000). This 'shape factor' (Eq. (2)) reduces both D_{max} and the associated stress intensity factor relative to those for a tall 2-D fracture (e.g. Lawn, 1993, pp. 31–33). The maximum displacement on an elliptical fracture (Eq. (1)) thus depends explicitly on both a and b (Irwin, 1962; Willemse et al., 1996; Gudmundsson, 2000). Eq. (2) can be approximated for fracture mechanics problems by a flaw shape parameter (Anderson, 1995, pp. 115–116) Ω:

$$E(a,b) = \Omega \cong \sqrt{1 + 1.464\left(\frac{a}{b}\right)^{1.65}} \qquad (3)$$

This approximation is within 5% of the numerical solution to Eq. (2) obtained from tabulated values listed in Beyer (1987), as demonstrated in Fig. 5. Ω can be substituted into Eq. (1) for $E(a,b)$, permitting calculation of D_{max} for arbitrary fracture lengths and aspect ratios.

For an elliptical fracture, the half-length parameter b in Eq. (1) must be modified to vary from a to b (Irwin, 1962; Kassir and Sih, 1966). Using the factor:

$$\sqrt{\sin^2\theta + \left(\frac{a}{b}\right)^2 \cos^2\theta} \qquad (4)$$

in which θ is the angle to a point on its tipline (Irwin, 1962; Kassir and Sih, 1966; Fig. 4b), the radius of the ellipse r (defined as the distance from the ellipse's center to a point on its tipline) is given by:

$$r = b\sqrt{\sin^2\theta + \left(\frac{a}{b}\right)^2 \cos^2\theta} \qquad (5)$$

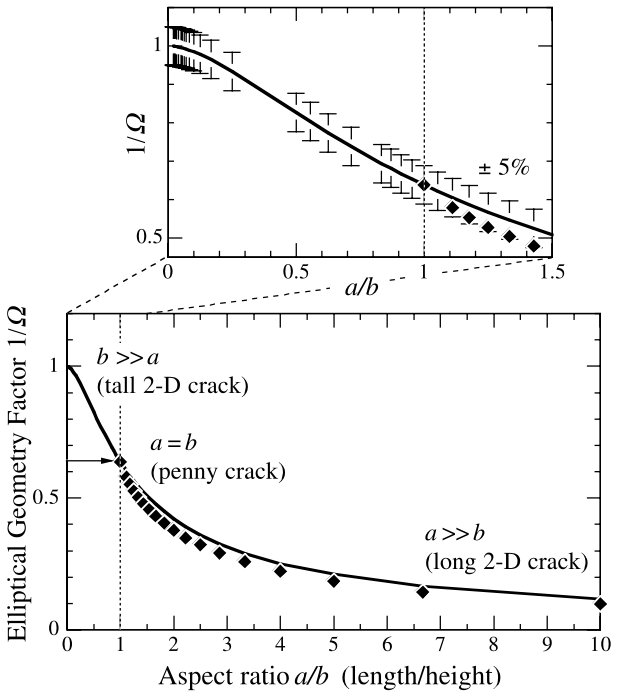

Fig. 5. Comparison of elliptical geometry factor $1/\Omega$ (solid line, Eq. (3); assumes half-length $a = 1$) and numerical solution of elliptic integral (filled symbols) as a function of fracture aspect ratio a/b. Upper panel shows detail for $a/b \leq 1.5$ with ±5% uncertainty in values of Ω.

The equation for maximum (relative) displacement on an elliptical fracture in an elastic medium, subjected to a uniform driving stress (and assuming negligibly small end zones in LEFM) is obtained by combining Eqs. (1), (3), and (5) to produce:

$$D_{max} = \left[\frac{2(1-\nu)}{G}\sigma_d\right]\left(\frac{b\sqrt{\sin^2\theta + \left(\frac{a}{b}\right)^2\cos^2\theta}}{\sqrt{1 + 1.464\left(\frac{a}{b}\right)^{1.65}}}\right) \qquad (6)$$

Eq. (6) reduces to 2-D cases for the limiting values of $r = a$ and $r = b$. For a slice along the fracture's horizontal axis (the $2a$ direction), $\theta = 0°$ and Eq. (5) yields a half-length of a. For a vertical slice (along the $2b$ axis), $\theta = 90°$ and Eq. (5) yields a half-length of b. Similarly, for a tall 2-D, plane-strain fracture (with $b \gg a$), the denominator (Eq. (3)) approaches 1.0; the increase in Eq. (3) with larger values of aspect ratio a/b (Fig. 5) controls the well-known reduction in D_{max} with elliptical geometry (specifically, with b/a; Irwin, 1962; Willemse et al., 1996). Eq. (6) implies that the D–L scaling of 3-D elliptical fractures depends on both length $2a$ and height $2b$.

3.2. End zone and effective driving stress

Consideration of end zones is important in 3-D D–L scaling for several reasons:

1. Most geologic fractures do not reflect conditions of small-scale yielding and LEFM (Cowie and Scholz, 1992b; Rubin, 1993) due to a combination of finite (small) rock strength at the tipline and relatively large ratios of driving stress to yield strength (e.g. Rubin, 1993). Measurements of the near-tip displacement profiles for joints and dikes (Rubin, 1993; Khazan and Fialko, 1995), faults (Dawers et al., 1993; Cartwright and Mansfield, 1998; Cowie and Shipton, 1998; Moore and Schultz, 1999), and deformation bands (Fossen and Hesthammer, 1997) reveal large departures from the ideal steep near-tip displacement gradients required by LEFM, such as tapered or linear displacement distributions, whose maximum values (D_{max}) are also smaller than those of an equivalent LEFM fracture.
2. End zones provide a physical basis for the linear displacement–length scaling of geologic fractures (Cowie and Scholz, 1992b). By replacing fracture toughness (having units of MPa $m^{1/2}$) by yield strength (having units of MPa), a linear (proportional) relationship between the maximum displacement and fault length (e.g. Clark and Cox, 1996) is achieved. D_{max} would scale with $L^{3/2}$, instead of L, for an LEFM fracture.
3. The effective driving stress σ_d^* associated with D_{max} on an elastic–plastic fracture depends on the length of the end zone, which in turn depends on both the ratio of driving stress σ_d (over the fracture's fully yielded part) to yield strength σ_y (over the end zone; Bilby et al., 1963; Heald et al., 1972; Chell, 1977; Li and Liang, 1986) and the fracture's aspect ratio (Chell, 1977). Although some workers specify particular values of end-zone length (e.g. Cowie and Scholz, 1992b; Martel and Boger, 1998), others treat it as a free parameter given uncertainties in actual values of driving stress σ_d or yield strength σ_y (e.g. Heald et al., 1972; Rudnicki, 1980; Li and Liang, 1986; Rubin, 1993; Bürgmann et al., 1994; Cooke, 1997; Martel, 1997). As a result, the effective driving stress σ_d^* acting on an elastic–plastic fracture depends explicitly on both a/b and σ_y/σ_d.

In this section we develop expressions for end-zone length around the tipline of an elliptical fracture as a function of aspect ratio a/b and end-zone strength σ_y/σ_d.

We build on the approach pioneered for 2-D plane problems by Dugdale (1960) and Barenblatt (1962) for mode-I cracks, Palmer and Rice (1972) for mode-II slip surfaces in overconsolidated soil, and Cowie and Scholz (1992b) for faults in rock. Although the near-tip deformation mechanisms invoked by Dugdale (1960) and Barenblatt (1962) were different (cohesive vs. plastic), the form of their results is applicable to fractures having non-LEFM 'end zones' in which the specific yielding mechanism may depend on the fracture displacement mode (e.g. Cowie and Scholz, 1992b; Rubin, 1993). Heald et al. (1972), Chell (1977), Turner (1979), Li and Liang (1986) and Ingraffea (1987) discuss applications of fractures with sizable (non-LEFM) end zones in engineering, whereas Rudnicki (1980), Li (1987), Martel and Pollard (1989), Cowie and Scholz (1992b), Rubin (1993), Bürgmann et al. (1994), Cooke (1997), Martel (1997), Cowie and Shipton (1998) and Willemse and Pollard (1998) apply the approach to 2-D fractures in rock. End zones around equidimensional, 'penny-shaped' fractures are calculated and discussed by Chell (1977) and Martel and Boger (1998). In all cases, fracture–surface displacements are modulated by end zones that are sufficiently large that the limiting LEFM solution is not appropriate. Mechanically, the end zones attain lengths that exceed the Irwin plastic-zone dimensions when the requirement for small-scale yielding conditions is relaxed (e.g. Kanninen and Popelar, 1985, pp. 282–283). This also modifies the shape of the relative-displacement distribution, from elliptical to bell-shaped or linear (e.g. Cowie and Scholz, 1992b; Bürgmann et al., 1994; Cooke, 1997).

We define the driving stress σ_d on a deformation band as $(\sigma_r - \sigma_i)$ and the yield strength σ_y of the end zone as $(\sigma_p - \sigma_i)$ (see Table 1 and Fig. 6). We associate the end zone bounding a deformation band with the area ahead of the band within which the porosity locally increases and

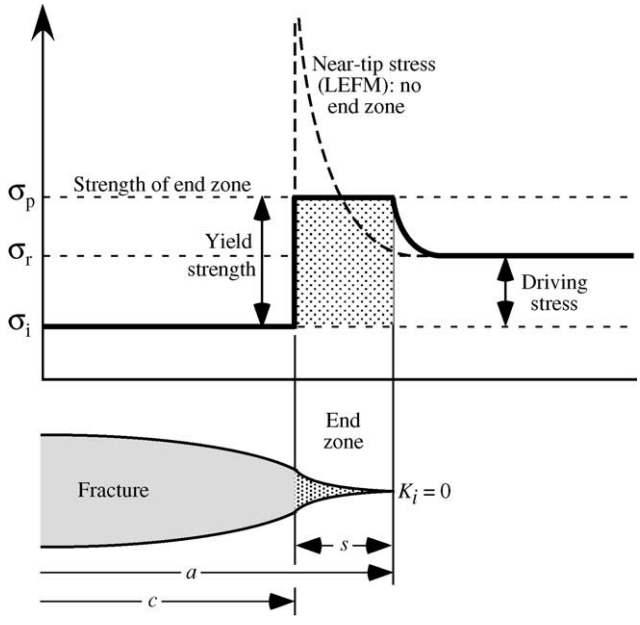

Fig. 6. Distribution of stress (resolved on the fracture plane) near the tip of an elastic–plastic fracture. Amplified stress due to fracture-wall displacements (dashed curves) decays with distance from fracture tip to σ_r in the surrounding unfractured rock. Length s of end zone is defined by a constant value of yield (peak) stress σ_p. Driving stress σ_d is the difference between resolved remote stress σ_r and internal boundary value σ_i (e.g. pore-fluid pressure or residual frictional strength). Yield strength σ_y is the difference between σ_p and internal boundary value σ_i.

grain fracturing (for cataclastic bands) begins (e.g. Aydin, 1978b; Antonellini et al., 1994) in response to amplified stresses near the band's tipline (Fig. 6).

Sizable end zones are associated with a reduction in the value of D_{max} on the fracture (e.g. Bürgmann et al., 1994) relative to the LEFM case that incorporates indefinitely strong (and negligibly small) end zones with a fracture of equivalent dimension. As emphasized by Rubin (1993), however, the length of an elastic–plastic fracture can be defined as either including or excluding the end zone (Fig. 7, central panel). The former case corresponds to the effective fracture length $L = 2(c + s) = 2a$ in LEFM, in which s is the length of the (small) plastic zone at the fracture tip and $a = (c + s)$ (see Fig. 7). Cowie and Scholz (1992b) adopt L as the effective fault length for D–L scaling, following Rudnicki (1980) and Palmer and Rice (1972). On the other hand, the latter case that defines the fracture length L^* by the 'unyielded' central portion (c), excluding the end zone (s), is commonly used in engineering fracture mechanics (e.g. Bilby et al., 1963; Heald et al., 1972; Chell, 1977), with $L^* = 2c$. In LEFM, $c \rightarrow a$, leading to little ambiguity in locating the fracture tip precisely, but this may not be the case for geologic fractures (e.g. Rubin, 1993). In this paper we adopt the total, effective length $L = 2(c + s)$, where s is the explicit, non-negligible length of the end zone whose length may exceed the (negligibly small) limiting value s given in LEFM.

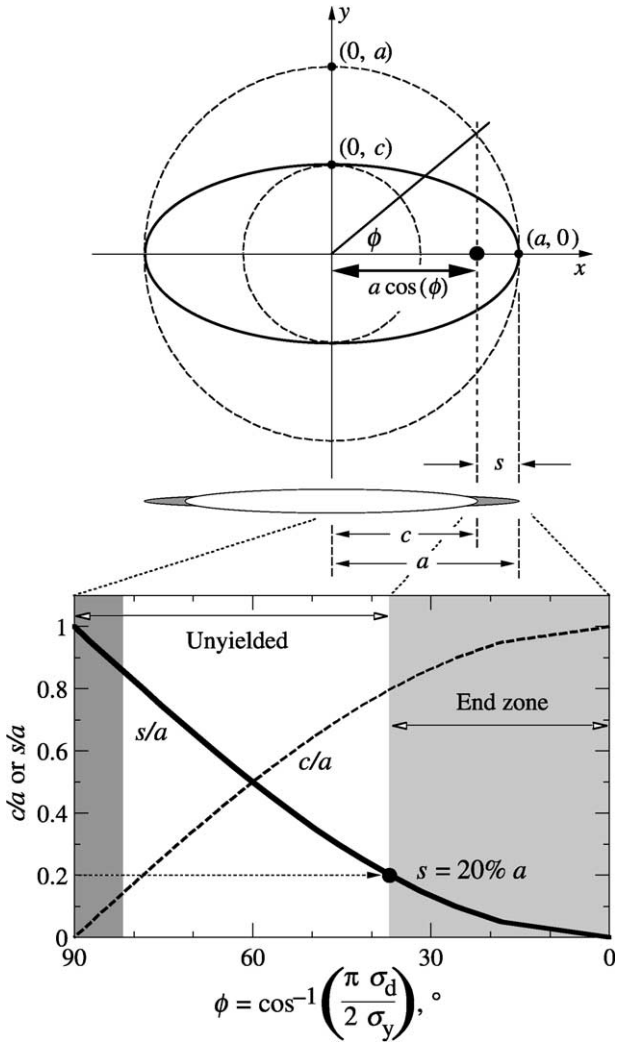

Fig. 7. Upper panel relates the quantity σ_d/σ_y to dimensions for yielded 2-D fracture half-length c, end zone length s, and total effective (elastic–plastic) fracture half-length a using the parametric angle $\phi = [(\pi/2)(\sigma_d/\sigma_y)]$ (after Kassir and Sih, 1966; Tada et al., 2000, p. 384). Lower panel shows dependence of s/a and c/a on σ_d/σ_y; $s/a \leq 0.2$ shaded; expressions valid for $s/a < 0.86$ and $\phi < 82°$ (dark shaded region).

In order to balance the singular near-tip elastic stresses generated near an ideal fracture (and to eliminate the LEFM singularity; Goodier, 1968), opposing stresses are defined (using a Dugdale-type 'cohesive' end zone conceptualization) to act across a narrow zone, coplanar with the fracture. The length s of the end zone associated with a 2-D fracture, written as the ratio of nonyielded (c) to effective (a) fracture lengths (Bilby et al., 1963; Heald et al., 1972; Chell, 1977), is:

$$\frac{c}{a} = \cos\left(\frac{\pi}{2}\frac{\sigma_d}{\sigma_y}\right) \tag{7a}$$

or explicitly,

$$\frac{s}{a} = 1 - \cos\left(\frac{\pi}{2}\frac{\sigma_d}{\sigma_y}\right) \tag{7b}$$

in which σ_d is the driving stress and σ_y is the (constant) yield strength of the surrounding rock ahead of the fracture tip (and in the end zone). The cosine function in Eqs. (7a) and (7b) relates the quantity σ_d/σ_y to the dimensions for nonyielded fracture c, end zone s, and total effective (elastic–plastic) fracture half-length a (Fig. 7, upper panel). For $\phi = [(\pi/2)(\sigma_d/\sigma_y)] = 0°$, $\sigma_y \rightarrow \infty$, $s \rightarrow 0$, and LEFM conditions apply (Fig. 7, lower panel, right-hand side). Smaller values of σ_y are associated with greater end-zone lengths and larger values of ϕ. These expressions are considered appropriate for $(\sigma_y/\sigma_d) > 1.1$ (Chell, 1977; Kanninen and Popelar, 1985, p. 283), implying maxima for $s/a < 0.86$ and $\phi < 82°$ (dark shaded region in Fig. 7, lower panel). For the particular case of $s = 0.2a$ adopted by Cowie and Scholz (1992b) for faults (light shading in Fig. 7), $\phi = 37°$.

End-zone length (Eq. (7b)) scales with driving stress and inversely with yield strength. As demonstrated in Fig. 8a, as the driving stress becomes small relative to the yield strength (i.e. $(\sigma_y/\sigma_d) > 10$), $c/a \rightarrow 1$ and $s/a \rightarrow 0$, approximating LEFM conditions (right-hand side of Fig. 8). However, as the driving stress becomes larger relative to the yield strength of the rock in the end zone, c/a decreases and the end zone grows relative to the total effective fracture half-length a. In this case, the effective driving stress acting

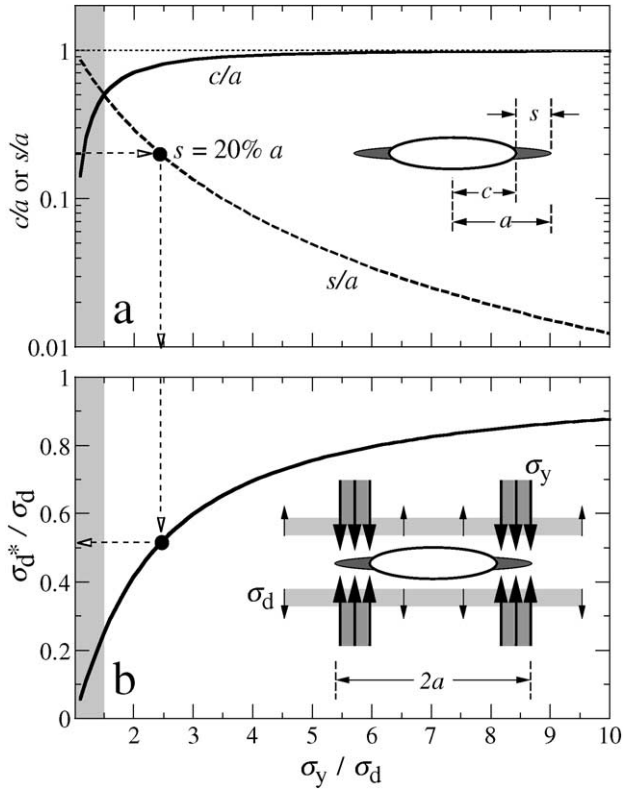

Fig. 8. (a) Dependence of end-zone length s on end-zone strength σ_y/σ_d. Solid curve for c/a, Eq. (7a); dashed curve for s/a, Eq. (7b). Dot indicates value of $\sigma_y/\sigma_d \approx 2.5$ for $s/a = 0.2$. (b) Dependence of the effective driving stress σ_d^*, normalized by the driving stress on an LEFM 2-D (tunnel) fracture σ_d, on the end-zone strength σ_y/σ_d. Dot shows $\sigma_d^*/\sigma_d \approx 0.5$; Eq. (8b) plotted.

over the elastic–plastic ('post-yield') fracture includes the competing contributions from the driving stress σ_d that acts over the entire length $L = 2a$, promoting relative displacement of the fracture walls, and from the opposing stresses within the end zone (defined by $\sigma_{ez} = (\sigma_d - \sigma_y)$; Table 1). We define an effective driving stress σ_d^* acting over the effective elastic–plastic fracture length $2a$, for 2-D fractures, as:

$$\sigma_d^* = \left[\sigma_d\left(\frac{c}{a}\right)\right] + \left[\sigma_{ez}\left(\frac{s}{a}\right)\right] \tag{8a}$$

in which a is a constant for the 2-D fracture. Using Eqs. (7a) and (7b) and rearranging, Eq. (8a) becomes:

$$\sigma_d^* = \sigma_d - \sigma_y\left[1 - \cos\left(\frac{\pi}{2}\frac{\sigma_d}{\sigma_y}\right)\right] \tag{8b}$$

The effective driving stress given by Eqs. (8a) and (8b) is implicitly defined for unit half-length a (see Fig. 7a). The effective driving stress for a 3-D elliptical fracture is given by:

$$\sigma_{de}^* = \left\{\frac{\sigma_d - \sigma_y\left[1 - \cos\left(\frac{\pi}{2}\frac{\sigma_d}{\sigma_y}\right)\right]}{\sqrt{\left(\cos^2\theta + \left(\frac{b}{a}\right)^2\sin^2\theta\right)\left(1 + 1.464\left(\frac{a}{b}\right)^{1.65}\right)}}\right\} \tag{9}$$

The term σ_d^* in Eqs. (8a) and (8b) corresponds to that used by Cowie and Scholz (1992a; see Table 1) and Scholz (1997) with, however, the explicit specification of an important variable coefficient. For the particular case discussed by Cowie and Scholz (1992b), $s = 0.2a$ and $\sigma_y/\sigma_d = 2.44$ (see Fig. 8), Eq. (8b) requires $\sigma_d^*/\sigma_d = 0.51$ (Fig. 8b). By explicitly evaluating the effective driving stress σ_d^* over the total effective (elastic–plastic) fracture length $2a$ using Eqs. (8a) and (8b), the decrease in D_{max} with increasing s (for a given fracture length $2a$ and shown explicitly by Bürgmann et al. (1994)), is related to the reduction in effective driving stress σ_d^* acting over the fracture relative to σ_d (see Fig. 8b). The discrepancy between the effective (σ_d^*) and LEFM-based driving stress (σ_d) increases with progressively smaller (weaker) values of yield strength. For example, the discrepancy in driving stress is ~10% for fractures having $s = 1\%$ of a (Fig. 7a; $s/a = 0.01$) and >50% for $s/a > 0.2$. This variable coefficient (the vertical scale in Fig. 8b) can be incorporated into the parameter C in the Cowie and Scholz (1992a) term for fracture shear strain, $\gamma = C(\sigma_y - \sigma_d)/G$ (see also Scholz, 1997). By explicitly considering the relationship between effective driving stress and end-zone length (Eq. (8b)), the curves for the curves for 3-D D–L scaling developed in this paper shift to smaller values than the approximate 2-D contours of γ (diagonal dashed lines in Fig. 1) by the factor σ_d^*/σ_d.

The change in geometry from 2-D (tunnel) to 3-D (penny) fractures is associated with a decrease in end-zone length relative to 2-D fractures (Fig. 9a). As shown in Fig. 9b, assuming the same values for fracture length ($2a$), driving stress, and yield strength, the end zone adjacent to a penny crack is consistently smaller than that bounding a 2-D tunnel crack. The smaller end-zone length is due to the greater constraint on deformation imposed on the penny crack by its fully bounded circular periphery, compared with the tunnel crack that is bounded only along its vertical edges (Chell, 1977; Martel and Boger, 1998). The reduction of end-zone length with fracture geometry is associated physically with a corresponding decrease in the value of maximum displacement D_{max} for the penny crack relative to the 2-D tunnel crack ($2/\pi$; e.g. Lawn, 1993, p. 32). Tall elliptical fractures ($b > a$) should have values of end-zone length intermediate between the tunnel and penny geometries (e.g. Fig. 9b).

By substituting Eq. (5) into Eq. (7b), the length of the end zone surrounding an elliptical fracture is given

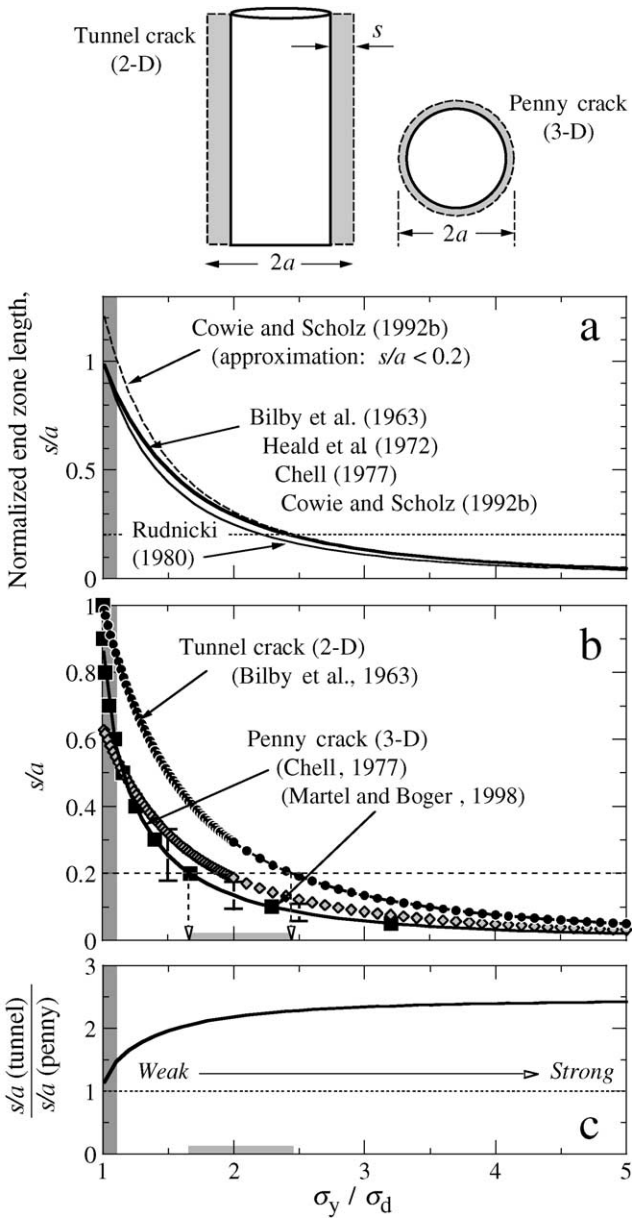

Fig. 9. (a) Comparison of theoretical end-zone lengths from the literature. Dashed line shows $s/a = 0.2$. (b) Fracture aspect ratio a/b reduces end-zone length at a given end-zone strength for 3-D (penny) fractures ($a/b = 1$; lower curve) relative to 2-D (tunnel) fractures ($b \gg a$; upper curve). Filled squares show values calculated by Martel and Boger (1998); coincident curve for penny fracture is from Chell (1977). Filled dots and diamonds show values calculated using Eq. (10) for tunnel and penny geometries, respectively; error bars show ±30% of Chell's (1977) and Martel and Boger's (1998) values for the penny geometry. (c) Relative length of end zone for tunnel fracture, compared with penny fracture, as a function of yield strength. Horizontal shaded bars in (b) and (c) indicate range of predicted end-zone strengths for length $s = 0.2a$. Vertical bars in (a), (b), and (c) show limits of validity for theoretical end-zone lengths ($\sigma_y/\sigma_d > \sim 1.1$).

approximately by:

$$s = \left[1 - \cos\left(\frac{\pi}{2}\frac{\sigma_d}{\sigma_y}\right)\right]\left(\frac{b\sqrt{\sin^2\theta + \left(\frac{a}{b}\right)^2\cos^2\theta}}{\sqrt{1 + 1.464\left(\frac{a}{b}\right)^{1.65}}}\right) \quad (10)$$

As shown in Fig. 9b, the predicted length is within ±30% of that for the penny fracture as given by Chell (1977) and Martel and Boger (1998). This difference is reasonable given the idealization of near-tip yielding within a volume as a planar zone (e.g. Bilby et al., 1963; Heald et al., 1972; Li and Liang, 1986; Engelder et al., 1993) and uncertainties of perhaps a factor of two for field estimates of the length of an equivalent planar end-zone (e.g. Cowie and Scholz, 1992b).

Because the magnitude of D_{max} is proportional to the level of driving stress acting on the fracture (e.g. Pollard and Segall, 1987; Eq. (1)), and for a given fracture size and yield strength, end-zone length increases with D_{max}. Longer end zones are generated to absorb the greater magnitudes of near-tip stress associated with larger values of D_{max}. Fractures of comparable length but with smaller values of D_{max} would require smaller end zones (e.g. Li and Liang, 1986).

4. Characteristics of the elliptical (3-D) elastic–plastic fracture

By combining the expressions for the maximum (relative) displacement on an elliptical fracture in an elastic medium (Eq. 6) with the effective driving stress for an elastic-plastic fracture (Eq. (9)), the 3-D displacement-length scaling relation becomes

$$D_{max} = \left[\frac{2(1-\nu)}{G}\right] \times \left\{\frac{\sigma_d - \sigma_y\left[1 - \cos\left(\frac{\pi}{2}\frac{\sigma_d}{\sigma_y}\right)\right]}{\sqrt{\left(\cos^2\theta + \left(\frac{b}{a}\right)^2\sin^2\theta\right)}\sqrt{1 + 1.464\left(\frac{a}{b}\right)^{1.65}}}\right\} \times \left(b\sqrt{\sin^2\theta + \left(\frac{a}{b}\right)^2\cos^2\theta}\right) \quad (11)$$

Scaling of maximum displacement and length for 3-D elliptical fractures (Eq. (11)) depends on the properties of the surrounding rock (modulus and Poisson's ratio), the end-zone length (through driving stress and yield strength), and the ellipse geometry (θ, a and b). The form of Eq. (11) is similar to previous 2-D formulations (e.g. Cowie and Scholz, 1992b) with the displacement–length ratio

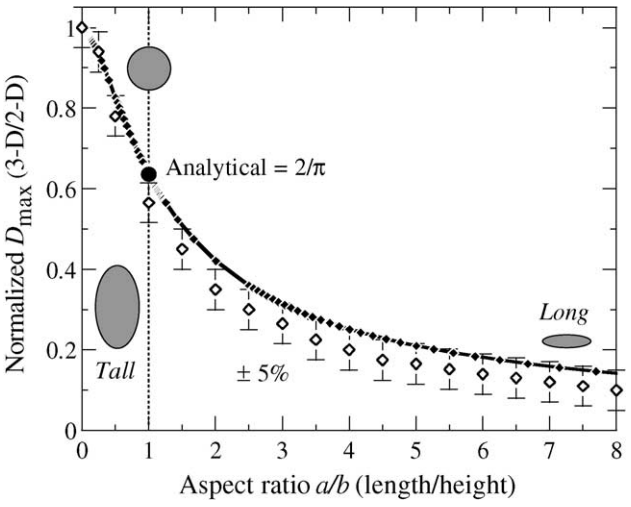

Fig. 10. Normalized maximum displacement (3-D relative to standard 2-D value) on a fracture decreases systematically with its fracture aspect ratio a/b. Filled symbols, 3-D scaling relationship from this paper (Eq. (11)); open symbols after Willemse et al. (1996) for $\nu = 0.25$. Shaded ellipses illustrate tall, circular, and long fractures that have the same value of length $2a$. Calculations assume $\sigma_y/\sigma_d = 50$, $\theta = 0°$, Poisson's ratio of 0.25, and shear modulus of 6.25 GPa.

proportional to the yield strength of the rock ahead of the fracture tipline and inversely proportional to modulus (G).

Eq. (11) extends the standard two-dimensional displacement–length scaling relation, for which fracture height $2b$ is not considered (because $2b \gg 2a$), to 3-D elliptical fracture geometries. D_{max} is an explicit function of fracture length and fracture height in Eq. (11). Because $a \neq b$ in general for natural fractures (e.g. Nicol et al., 1996; Gudmundsson, 2000), displacement–length scaling relations will necessarily depend on which length scale is chosen: the horizontal length or the vertical height. The relationship (Eq. (11)) assumes that the yield strength does not vary significantly along the fracture periphery (Chell, 1977), which appears reasonable for small fractures but perhaps not for fractures large enough to transect differing rheologies or for strongly interacting fractures (e.g. Gupta and Scholz, 2000).

4.1. Variations in the main parameters

Willemse et al. (1996) compared the predicted values of D_{max} for elastic 2-D and 3-D cases that assume negligibly small end zones (i.e. LEFM conditions). They showed that D_{max} decreases systematically with increasing fracture aspect ratio (a/b) but they did not develop the implications for displacement–length scaling in further detail. The particular values treated by Gudmundsson (2000) for tall ($b \gg a$), circular ($a = b$), and long ($a \gg b$) fractures also match those used by Willemse et al. The scaling relationship for elliptical fractures defined in this paper (Eq. (11) with negligibly small end zones) compares favorably with the results reported by Willemse et al. (1996), as shown in Fig. 10. Relative to an indefinitely tall 2-D fracture ($b \gg a$), a penny fracture can accommodate only about 60% ($2/\pi$) of the displacement on the tall fracture (large dot on Fig. 10), whereas an indefinitely *long* 2-D fracture ($a \gg b$) can accommodate less than one-tenth of the displacement on the tall fracture of the same size (e.g. for $a/b > 8$ in Fig. 10). As a result, standard 2-D approaches to displacement–length scaling that neglect the effect of fracture height ($2b$) may systematically *overpredict* the magnitude of D_{max} on a particular fracture by at least an order of magnitude. These errors will propagate through the population statistics if aspect ratio is not explicitly accounted for.

The end-zone length (Eq. (10)) varies as a function of position along the elliptical tipline, as shown in Fig. 11a for several values of end-zone strength (σ_y/σ_d). The length at any point along the tipline depends additionally on that fracture's aspect ratio. For example, s is maximum for long fractures ($a/b = 10$) along the vertical, semi-minor ($\theta = 90°$ and $r = b$) axis and minimum along the horizontal direction (semi-major axis, $\theta = 0°$ and $r = a$). For tall fractures (Fig. 11b; inset to Fig. 11), s is maximum along the horizontal direction ($\theta = 0°$ and $r = a$). Comparison with commonly cited values for s/a of ~0.1–0.2 (shaded bar in Fig. 11a and b) suggests that knowledge of both the position along a fracture's tipline (θ) and the fracture aspect ratio (a/b) would be necessary to interpret the significance of end-zone length for a given value of strength.

The ratio of maximum displacement D_{max} to fracture length L depends on both the position along the tipline (Fig. 11c) and the fracture's aspect ratio (Fig. 11d). D_{max}/L is maximized on fractures with stronger end zones and minimized on those with weak end zones, supporting previous suggestions (Cowie and Scholz, 1992b; Martel, 1997; Moore and Schultz, 1999; Schultz, 1999; Wibberley et al., 2000) that the yield strength of an end zone can modulate the displacement–length scaling relations. Measurement of D_{max} and L in either map view or cross-section, for the same fracture, can produce substantial variation in D_{max}/L due to its sensitivity to the fracture's aspect ratio.

4.2. The *D–L* diagram for 3-D fractures

The 3-D scaling relationship (Eq. (11)) can be plotted on the standard log–log D_{max}/L diagram (Fig. 12, for horizontal trace lengths, $\theta = 0°$). Tall fractures ($L \ll 2b$) define a positive 45° (1:1) slope (left side of diagram, dashed lines) because D_{max} depends only on the length L (and not on the height $H = 2b$, for given values of modulus and Poisson's ratio). The change in slope on the D–L diagram, from 1:1 to shallower slopes, is related to the sensitivity of D–L scaling of 3-D elliptical fractures to the fracture height $2b$ (e.g. Willemse et al., 1996; Gudmundsson, 2000; Fig. 10). As a fracture grows in length at constant height, its ability to accommodate displacements degrades with increasing

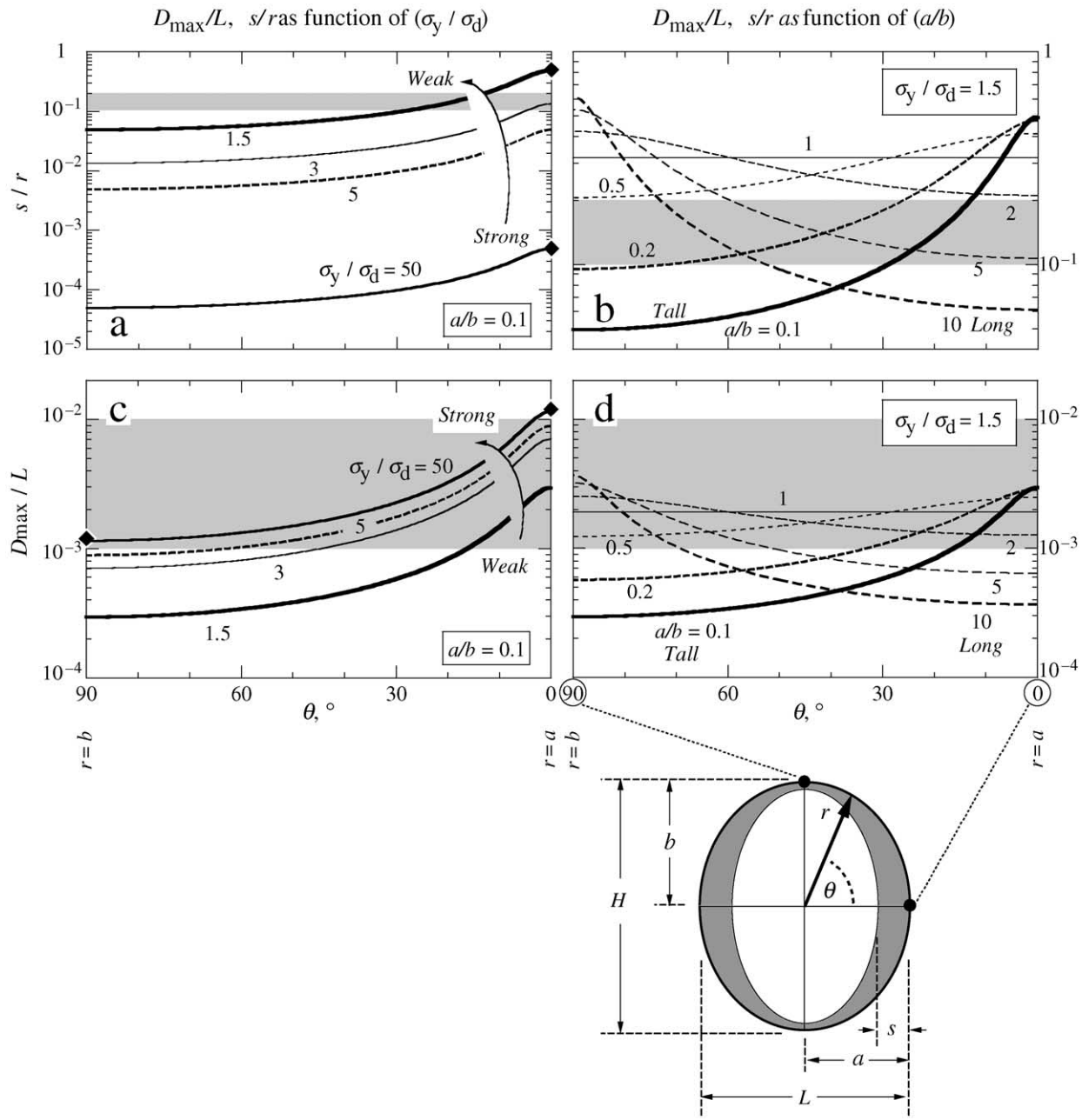

Fig. 11. Diagrams showing how end zones and maximum displacement/length ratio vary systematically with position along an elliptical fracture tipline and with fracture aspect ratio. Upper row displays variation in end-zone length (Eq. (10)) with (a) end-zone strength, and (b) fracture aspect ratio, both as a function of position along tipline of elliptical fracture. Shaded band in (a) and (b) shows typical range of end-zone lengths from the literature ($0.1 < s/a < 0.2$). Lower row displays variation in maximum displacement/length ratio with (c) end-zone strength, and (d) fracture aspect ratio, as a function of position along tipline. Shaded band in (c) and (d) shows typical range of displacement–length ratios for faults (e.g. Fig. 1). All calculations assume a yield strength of 10 MPa ($\sigma_y/\sigma_d = 10$), Poisson's ratio of 0.25, and shear modulus of 6.25 GPa.

aspect ratio, leading to slopes shallower than 1:1 on the D–L diagram (right-hand side of Fig. 12).

A family of D–L curves (calculated by using Eq. (11)) describes how maximum displacements on 3-D fractures of various heights scale with their map lengths (Fig. 12). The point on each curve that corresponds to an aspect ratio $a/b = 1$ (equidimensional or 'penny-shaped' fracture geometry) defines the transition from a normal (1:1) and constant slope to a shallower, nonlinear slope. Interestingly, connecting the points on different curves for the same value of aspect ratio (dots in Fig. 12b) produces a straight line, with a constant slope of 1.0. Other parallel lines can be constructed for other values of fracture aspect ratio (e.g. line for $a/b = 10$ in Fig. 12b). These lines defined by constant values of fracture aspect ratio describe fractures in a population that grow in a self-similar, proportional manner; i.e. at a constant aspect ratio. In 2-D D_{max}/L scaling, these lines are related to the constant of proportionality γ

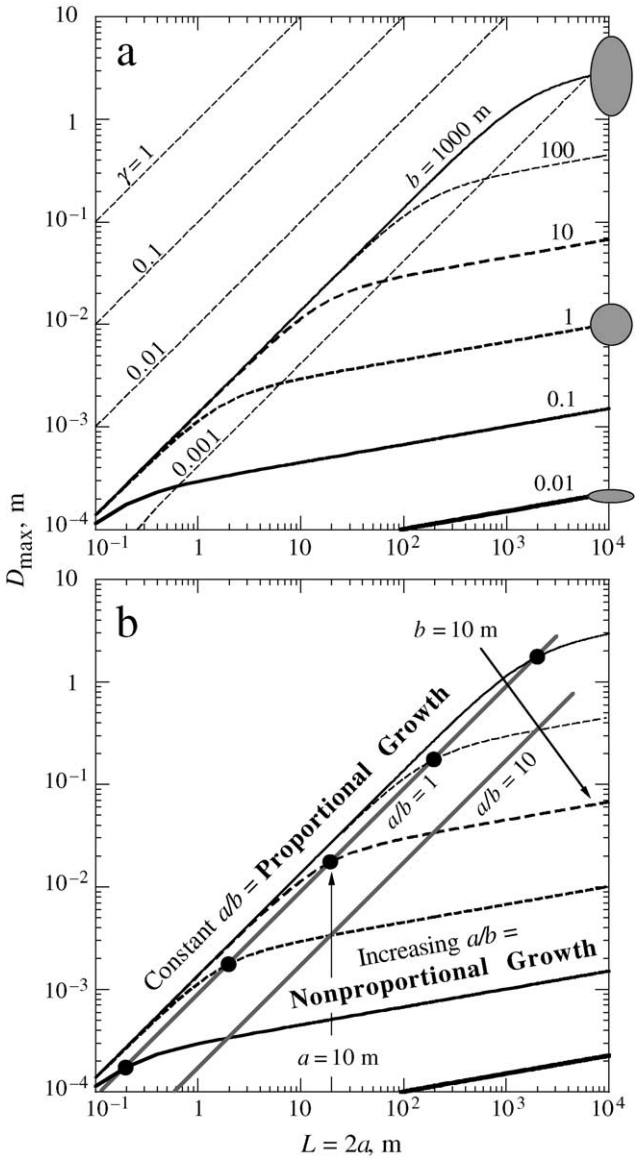

Fig. 12. Displacement–length scaling as a function of both fracture length ($L = 2a$) and height ($H = 2b$). (a) Theoretical values of $L = 2a$ are plotted as curves for particular values of fracture half-height ($0.01 \le b \le 1000$ m). Diagonal dashed lines show 2-D fracture shear strains calculated using effective driving stress ($\sigma_d^*/\sigma_d = 0.4142$, Eq. (9)) for $\sigma_y/\sigma_d = 2.0$ ($s = 0.3a$; Fig. 8). (b) Lines of constant aspect ratio are defined by points along each curve having a/b = constant (filled symbols, $a/b = 1$). Calculations assume $\sigma_y/\sigma_d = 2.0$, $\theta = 0°$, Poisson's ratio of 0.4, and shear modulus (see Section 4.2) of 1.6 GPa ($G/\sigma_d = 80.3$).

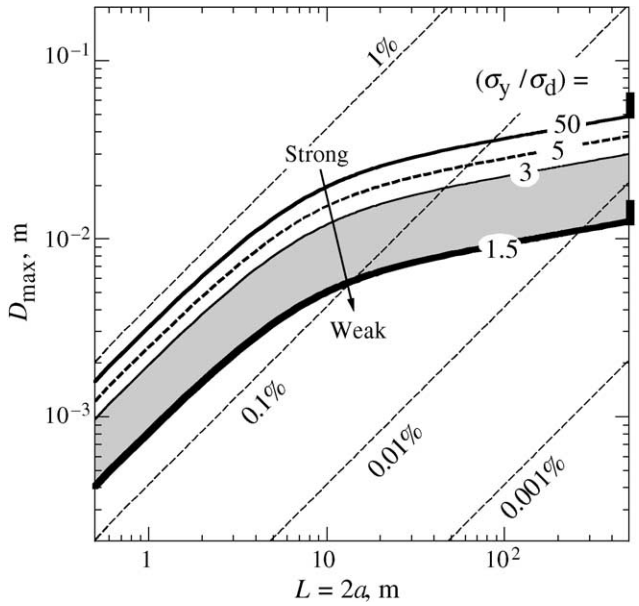

Fig. 13. Dependence of D–L scaling on end zone strength, σ_y/σ_d, for constant fracture height ($2b = 10$ m). Calculations assume $\sigma_y/\sigma_d = 50$ (strong end zone), 5 (for $\alpha = 0.005$), 3, and 1.5 weak end zone) with $\theta = 0°$, Poisson's ratio of 0.4 (bars on right border show 14% increase in values of curves for 50% change in ν to 0.2), and shear modulus of 1.6 GPa ($G/\sigma_d = 80.3$). Diagonal lines are contours of shear strain for 2-D fractures as in Fig. 12. Shaded area shows plausible range of end zone strengths for faults and deformation bands.

between D_{max} and L (e.g. Cowie and Scholz, 1992b). In 2-D cases, the aspect ratio implicitly remains constant during fracture growth or for all members of the population because only the fracture length (and not its height) is considered. As Fig. 12 shows, the linear relationship in 2-D between D_{max} and L is a special case of 3-D scaling that occurs for geometrically self-similar fractures (i.e. constant aspect ratio, proportional growth).

The curves shown in Fig. 13 demonstrate how the maximum displacement for 3-D elliptical fractures varies (with L and a for given value of b) for a range of end zone yield strengths σ_y. D_{max} shifts downward on the diagram (to smaller maximum displacements) for weaker end zones (at given values of L and $2b$; labeled curves in Fig. 13), in accord with previous investigations of 2-D scaling (e.g. Cowie and Scholz, 1992b). For a given fracture height $2b$, fractures of length $L = 2a$ can build up greater values of maximum displacement as end-zone strength increases. However, the horizontal position of the inflection point in the curve ($a = b$) is unchanged. For example, very strong end zones ($\sigma_y/\sigma_d = 50$), approximating LEFM conditions and small-scale yielding ($s/a \to 0$), are associated with values of D_{max} ~4 times greater than comparable fractures that are bounded by weak end zones ($\sigma_y/\sigma_d = 1.5$). Thus, fractures in a strong rock, like granite, could accommodate larger displacements than those having identical dimensions and driving stresses in a soft rock like a sandstone (given comparable values of modulus and Poisson's ratio for both rock types). For an actual fracture of given length and height, D_{max} will reflect a balance between end zone strength, driving stress, and rock properties (e.g. Eq. (11)).

Lines of constant D_{max}/L ratio obtained from 2-D D-L scaling relations (Cowie and Scholz, 1992b; Clark and Cox, 1996) correspond to contours of fracture shear strain, $\gamma = C(\sigma_y - \sigma_d)/G$ (Cowie and Scholz, 1992b; Scholz, 1997). A fracture population that follows $\gamma = 0.01$ would

be characterized by values of maximum displacement that scale linearly with fracture length, with $\gamma = 0.01$ corresponding to a fracture shear strain (Jamison, 1989; Wojtal, 1989) of 1%.

The fracture shear strain that is accommodated in an elliptical fracture's plane is given using the 3-D scaling relations by $D_{max}/L = \alpha$. Specifically:

$$\frac{D_{max}}{L} = \alpha \tag{12a}$$

in which

$$\alpha = \left[\frac{(1-\nu)}{G}\right].C_e \times \left\{\frac{\sigma_d - \sigma_y\left[1 - \cos\left(\frac{\pi}{2}\frac{\sigma_d}{\sigma_y}\right)\right]}{\sqrt{\left(\cos^2\theta + \left(\frac{b}{a}\right)^2 \sin^2\theta\right)}\sqrt{1 + 1.464\left(\frac{a}{b}\right)^{1.65}}}\right\} \tag{12b}$$

and L being given by twice the term r from Eq. (5) in Eq. (12a). The dimensionless fracture shear strain (Eq. (12b)) increases with driving stress, end zone yield strength, and Poisson's ratio, and decreases with modulus and fracture aspect ratio. Values of fracture strain also depend on the position around the fracture tipline; for strain in the horizontal plane, $\theta = 0°$.

We note that the values of fracture shear strain γ in the 2-D approach also depend on the end-zone length, the maximum displacement, and, in turn, on the effective driving stress on the elastic–plastic fracture (Eq. (9)). In their study of faults, Cowie and Scholz (1992b) inferred driving stresses in the order of 100 MPa and a shear modulus of 10 GPa (resulting in $G/\sigma_d = 100$). Smaller driving stresses (or 'stress drops,' e.g. <1 MPa; Martel and Pollard, 1989) may be used to represent individual seismic slip events having $D_{max}/L \approx 10^{-3}$–$10^{-5}$, whereas the larger cumulative geologic offsets on faults (Scholz, 1997) having $D_{max}/L \approx 10^{-1}$–$10^{-3}$ may be represented by cumulative driving stresses on the order of 100 MPa (e.g. Cowie and Scholz, 1992b). Using Eq. (11), the factor C required in the expression for γ (e.g. Scholz, 1997) is incorporated either by adjusting the magnitudes of the driving and yield stresses σ_d above 1 MPa (e.g. $\sigma_d = 100$ MPa and $\sigma_y = [(\sigma_y/\sigma_d) \times \sigma_d] = (1.5 \times 100) = 150$ MPa) or by reducing the modulus by an equivalent amount (e.g. $G/100 = 16$ MPa). The factor C_e and Eqs. (12a) and (12b) allows more precise values of fracture strain to be obtained from the D–L scaling relations.

Constant values of γ (and constant 45° slopes on the D–L diagram) are obtained for 3-D elliptical fractures that are tall compared with their lengths ($2b \gg L$; see Fig. 13, dashed diagonal lines, left-hand side of diagram). The constant slopes imply that the tall 3-D fractures approximate 2-D ones that scale with length only, independently of their heights. The values of γ are influenced by the strength of the fracture's end zone (Eqs. (12a) and (12b)). For given values of driving stress and rock-mass properties (modulus, Poisson's ratio appropriate for sandstone; see caption to Fig. 12 for values), a weak end zone ($\sigma_y/\sigma_d = 1.5$) leads to $D_{max}/L = \alpha = 0.0017$, or 0.17% (bold curve in Fig. 13). D–L ratios increase for stronger end zones by a factor of ~4 at $\sigma_y/\sigma_d = 50$, appropriate to an LEFM fracture in perfectly elastic surroundings (Fig. 8). For end zone strengths between 1.5 and 2.5 (see Fig. 8), the D–L ration varies by ±50%.

The value of fracture shear strain (Eqs. (12a) and (12b)) accommodated by a fracture population described by the 3-D scaling relation remains constant for a given value of end-zone strength (other parameters held constant). However a constant fracture shear strain is not achieved for stratibound fractures (a/b ≠ constant) because the slope of the D–L relation is nonlinear. This result parallels the decrease in a fracture's ability to accommodate displacements as its aspect ratio increases (Willemse et al., 1996; Fig. 10) and implies that, in general, a fracture's shape (a, b) must balance its maximum displacement (D_{max}) for a constant fracture strain to be maintained within a population.

In summary, for fractures that are much larger in height than in length ($a \ll b$; left side of Fig. 14), the shorter (length) dimension controls the magnitude of displacement on the 'tall' fracture (e.g. Gudmundsson, 2000). In this case, D_{max} and L scale linearly, and 2-D scaling relations and

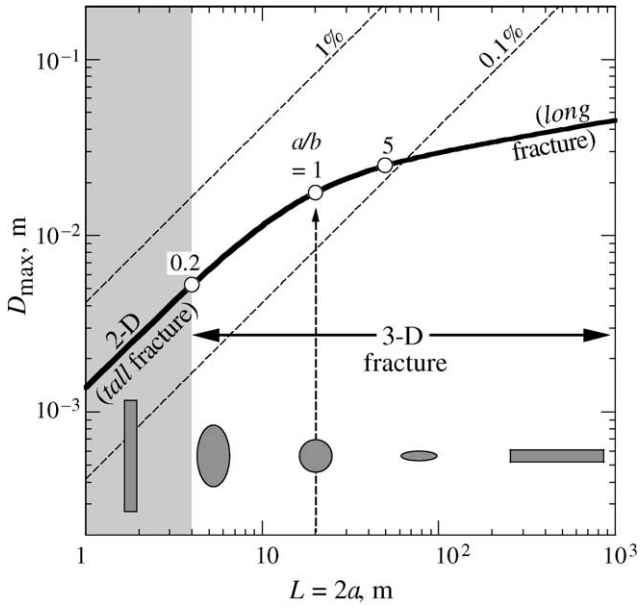

Fig. 14. Comparison between 2-D and 3-D scaling relations. The 3-D results converge toward the 2-D values of γ (fracture shear strain, dashed lines in shaded region) for tall fractures ($a/b \ll 0.2$). Curve shown calculated using $D_{max}/L = 0.00275$, $b = 10$ m, $\sigma_y/\sigma_d = 2.0$, $\theta = 0°$, Poisson's ratio of 0.4, and shear modulus of 1.6 GPa ($G/\sigma_d = 80.3$).

analyses such as those in use in the literature apply (e.g. Cowie and Scholz, 1992b; Bürgmann et al., 1994; Cladouhos and Marrett, 1996; Clark and Cox, 1996; Schlische et al., 1996). For long fractures ($a \gg b$; right side of Fig. 14), the smaller fracture height dominates the control on displacement, leading to a shallower, nonlinear slope on the D_{max}/L diagram (Fig. 14). Three-dimensional scaling relations apply where length is more than ~5 times the height (i.e. $a/b > 0.2$; unshaded region of Fig. 14).

5. Application to deformation bands in Utah

The deformation bands that are confined to layer e_1 of the Entrada Sandstone define a characteristically shallow slope (<1) on the D–L diagram (Fossen and Hesthammer, 1997) over the full range of band lengths. This data set, which motivated the 3-D analysis of D–L scaling, allows the predictions of population strain and displacement–length scaling of elliptical fractures to be tested against field data.

In order to independently evaluate the predictions of fracture strain from the 3-D scaling relationship (Eq. (12b)), we measured the frequency and normal dip-slip offsets of a representative sample of unfaulted deformation bands from the outcrop (Figs. 2b and c and 3a). Fifty-eight bands were measured along a 50-m-long linear (and horizontal) traverse oriented at 220° (Fig. 15b and c), normal to the strike of the fault surface (that nucleated within a cluster of deformation bands) shown in Fig. 3e. The bands define two complementary (conjugate) sets of orientations striking ~280° and dipping 60–85° NE and SW (Fig. 15a), and plane subhorizontal extension along the direction perpendicular to the mean azimuth of the bands (200 ± 10°; star in Fig. 15a). Using the calculated horizontal components of offset obtained from the strike (e.g. Peacock and Sanderson, 1993; Priest, 1993, pp. 96–97) and dip of each band, we find a cumulative extensional (horizontal) strain of 0.12% (Fig. 15c) along 200° (star in Fig. 15c).

In order to compare the fracture shear strains from the population statistics to the measured strain along the traverse, the predicted band-parallel fracture shear strains α (Eqs. (12a) and (12b)) are converted to the horizontal fracture strains ϵ_h by using:

$$\epsilon_h = \alpha(\cos\delta) \tag{13}$$

in which δ is the average dip of the bands and $\theta = 0°$ (in Eq. (11)). Using the average dip angle of 65° measured along the traverse, the horizontal (extensional) component of the fracture strain ϵ_h is reduced to 43% of the band-parallel fracture shear strain α. We varied the parameters in Eqs. (12a) and (12b) to determine the range of values consistent with the D–L scaling relations (Fossen and Hesthammer, 1997) and horizontal strain measured independently along the traverse. To achieve a horizontal fracture strain ϵ_h of 0.12%, the values are $3.0 < E < 5.0$ GPa (corresponding to a shear modulus G of 1.1–1.8 GPa), $0.2 < \nu < 0.4$, $1.5 < \sigma_y/\sigma_d < 2.5$, and $60° < \delta < 70°$. The variations listed for Young's modulus E (±25%), Poisson's ratio (±50%), end zone strength σ_y/σ_d (±25%), and band dip angle (±10%) collectively

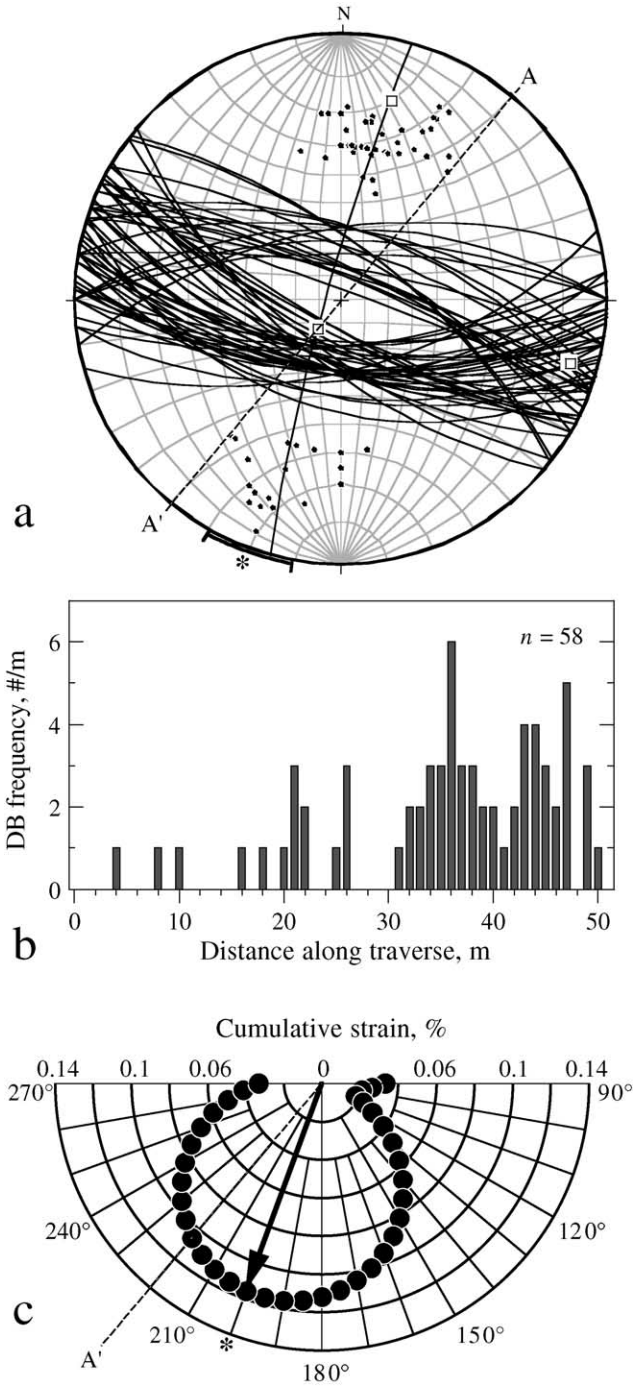

Fig. 15. (a) Equal-angle stereonet showing planes and poles to 58 deformation bands measured along traverse (see Fig. 2b). Cylindrical best-fit shown as great circle oriented at 200 ± 10° azimuth (star). Dashed line A–A′ shows 220° orientation of horizontal traverse line. (b) Frequency of deformation bands along NE–SW traverse, averaging 1.16 bands/meter. (c) Graphical solution for azimuth containing maximum cumulative strain (star and arrow) relative to orientation of traverse (dashed line A–A′).

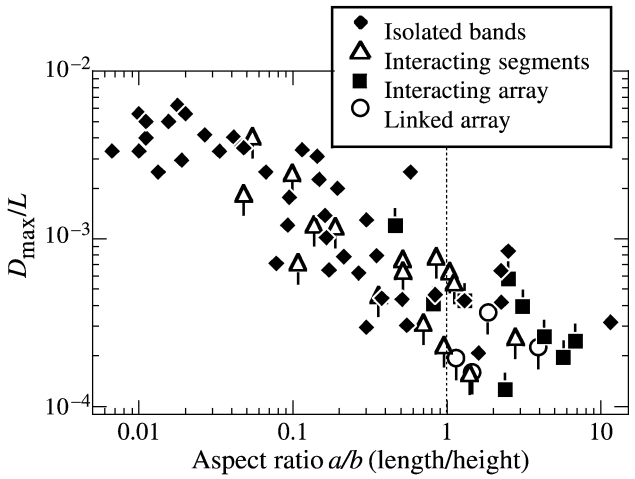

Fig. 16. D_{max}/L data for deformation bands plotted as a function of fracture aspect ratio a/b, indicating dependence of D_{max}/L scaling of deformation bands on fracture shape rather than just their lengths ($L = 2a$). Data from Fossen and Hesthammer (1997). Tick marks on symbols show direction of qualitative uncertainties in D_{max} associated with linkage geometries.

lead to an uncertainty in ϵ_h of less than a factor of two. The horizontal fracture strain can be increased by using shallower dips, smaller modulus, smaller Poisson's ratio, and/or stronger end zones. Increasing the modulus by a factor of 10 (keeping band dip and Poisson's ratio constant, as above) also predicts the strain value (0.12%) as long as the driving stress is also increased by a factor of 10, so that $G/\sigma_d = 80.3$ in both cases. However, increasing the end-zone strength to LEFM levels ($\sigma_y/\sigma_d > 50$) is not sufficient by itself to balance the larger value of G and thereby predict the same value of fracture strain (0.12%). Given particular values of rock properties (G, ν) and end zone strength (σ_y/σ_d), the driving stress σ_d must be varied to predict particular values of fracture strain using Eq. (11).

The 73 measurements of D_{max} and L reported by Fossen and Hesthammer (1997) from the 9-m-thick layer within the Entrada Sandstone ('e_1' in Figs. 2c and 3) are plotted as a function of aspect ratio in Fig. 16 (using a maximum thickness $2b$ of the porous sandstone layer of 9 m). Values of D_{max}/L that are independent of aspect ratio, and hence the vertical fracture height, would cluster about horizontal lines on the diagram; such clustering is not observed. In contrast, the data suggest a reduction in D_{max}/L with increasing values of fracture aspect ratio a/b by a factor of at least 5–10, particularly for aspect ratios greater than one. We infer that the 3-D fracture geometry influences D_{max}/L ratios within the study area.

Deformation bands coded by their map-view geometry (on the subhorizontal surface of the outcrop (Fig. 3a); Fossen and Hesthammer, 1997) are shown in Fig. 16. Isolated deformation bands (filled diamonds in Fig. 16) are widely separated from other bands. The lengths of closely spaced bands that interact mechanically with others (called 'soft-linked' in the literature) to form stepovers and eye structures (Cruikshank et al., 1991; Antonellini and Aydin, 1995; Fossen and Hesthammer, 1997) are difficult to assess precisely without quantifying the degree of interaction for each band segment (e.g. Segall and Pollard, 1980). Band segments in a soft-linked array plotted by using their individual lengths (open triangles in Fig. 16) exhibit excessive values of D_{max} for their lengths (tick marks adjoining symbols in Fig. 16) because the influence of the other segments is not included (e.g. Segall and Pollard, 1980; Willemse, 1997). On the other hand, the aggregate length of the interacting array (open circles in Fig. 16) will appear underdisplaced relative to a continuous band of equivalent length. Linked arrays of deformation band segments ('hard-linked systems'; filled squares in Fig. 16) may also exhibit somewhat smaller values of D_{max} than found for continuous bands with the reduction related to the degree of roughness and linkage history of the band. Additional uncertainties could be added to all four groups of deformation bands to account for linkage geometries in the vertical, down-dip direction given appropriate observations (not available from the study area).

The data replotted on a traditional displacement–length diagram (Fig. 17) show that a power-law slope of approximately 0.5 (heavy line in Fig. 17a) could be used to describe the population (Fossen and Hesthammer, 1997, 1998). This best-fit slope of 0.5 (Fossen and Hesthammer, 1997) is significantly shallower than power-law slopes of 1.0 (dashed line in Fig. 17a) inferred for faults from a wide range of rock types (Cowie and Scholz, 1992a; Clark and Cox, 1996). We infer that the shallower slope occurs because the deformation bands—as a population—do not maintain a constant aspect ratio over the length scale shown.

According to the calculations reported by Willemse et al. (1996) and others, fractures having heights less than 3–5 times their lengths should scale as 3-D surfaces. Inspection of Fig. 17a shows that bands having $L < \sim 3$ m, or 1/3 the stratigraphic thickness, may be qualitatively consistent with the 2-D proportional growth slope of 1.0 (dashed line in Fig. 17a). Proportional growth of penny-shaped fractures ($a = b$) would follow a slope of 1.0, as demonstrated in Fig. 13b, by cutting across curves for different values of b. Because the slopes of the proportional and nonproportional curves are parallel for aspect ratios less than one, however, it may not be possible to distinguish between them for this range of relative lengths using statistics alone (see also Fig. 14). On the other hand, the scaling of longer deformation bands is consistent with nonproportional growth and constant fracture height. Given these uncertainties, we conclude that nonproportional growth will be most clearly demonstrated on a D_{max}/L diagram for fractures having aspect ratios greater than one (Fig. 17b); when

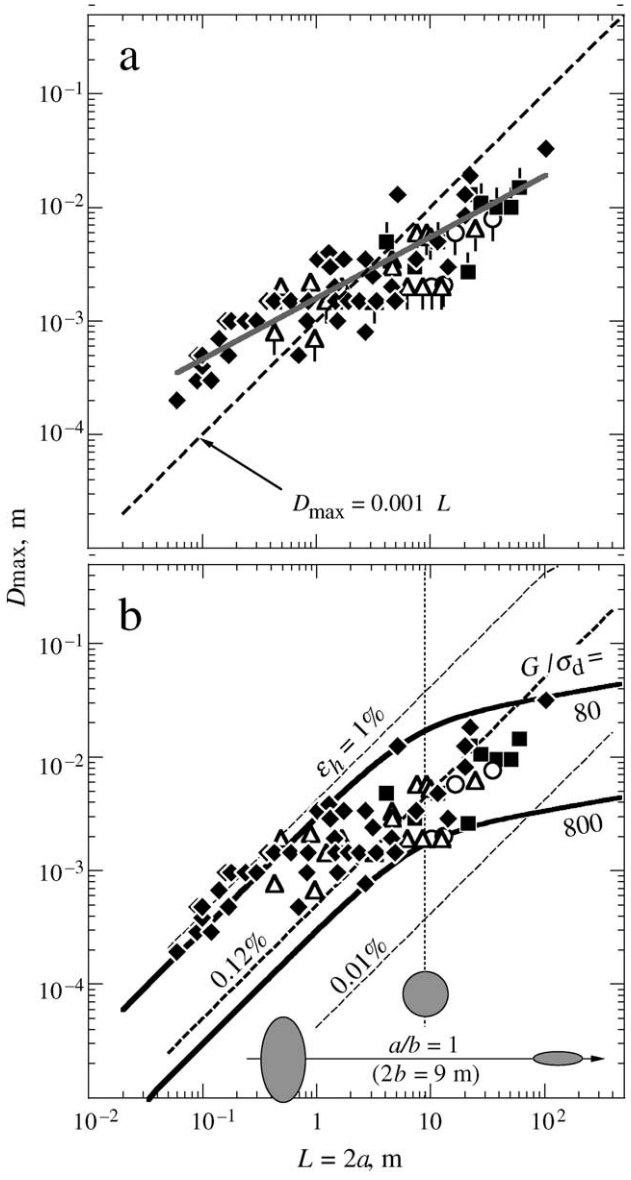

Fig. 17. Displacement–length scaling of deformation bands (data from Fossen and Hesthammer, 1997); symbols and tick marks as in Fig. 16. (a) Linear fits to the data; proportional growth curve (dashed line, slope = 1.0), least-squares regression (gray curve), $D_{max} = 0.002\ L^{0.56}$, $r^2 = 0.775$. (b) 3-D scaling relations fitted to the data calculated using Eq. (11) with $2b = 9$ m, $\sigma_y/\sigma_d = 2.0$, $\theta = 0°$, Poisson's ratio of 0.4, $\delta = 65°$ and shear modulus of 1.6 GPa ($G/\sigma_d = 80.3$). Gray curve shows value of horizontal fracture strain from traverse (0.12%).

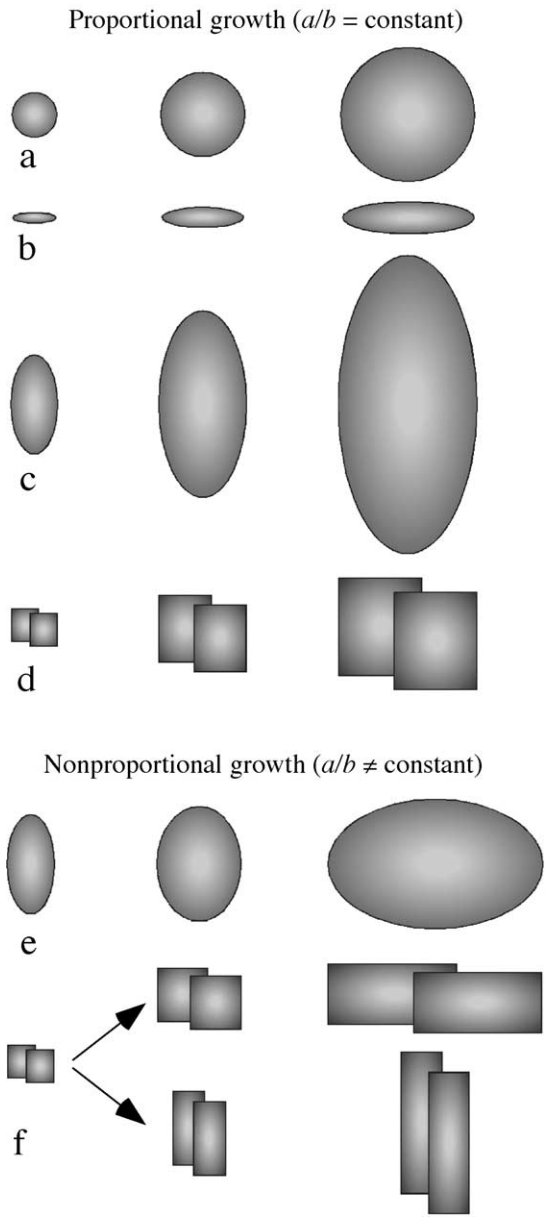

Fig. 18. Examples of fractures growing at constant aspect ratio (proportional growth, (a)–(d)), for which traditional D_{max}/L scaling relationships and constant slopes of 1.0 may apply, and fractures growing with increasing aspect ratio ((e) and (f)). Ellipses represent individual fracture surfaces, rectangles are interacting and/or linked fracture segments.

combined with shorter fractures of the same population, the aggregate power-law slope for the data set will be less than one.

The value of horizontal fracture strain obtained from the traverse (0.12%) agrees with the range predicted for the deformation band population from the 3-D analysis (Fig. 17b) using the parameters noted above. Given this correspondence, the yield strength of the end zones bounding deformation bands in the study area is probably small ($\sigma_y/\sigma_d < 2.5$; see Figs. 8 and 13). Significantly larger values of end-zone strength would be associated with steeper near-tip displacement gradients (see Fossen and Hesthammer, 1997, for measurements) and with pervasive secondary structures nucleating near the tips (e.g. Cooke, 1997) of individual, isolated bands; neither of these is observed in the study area. A ratio of shear modulus to driving stress (G/σ_d) of 80–800 is implied by the values of fracture strain, end-zone strength, and linkage geometry (Figs. 16 and 17) for the population of deformation bands.

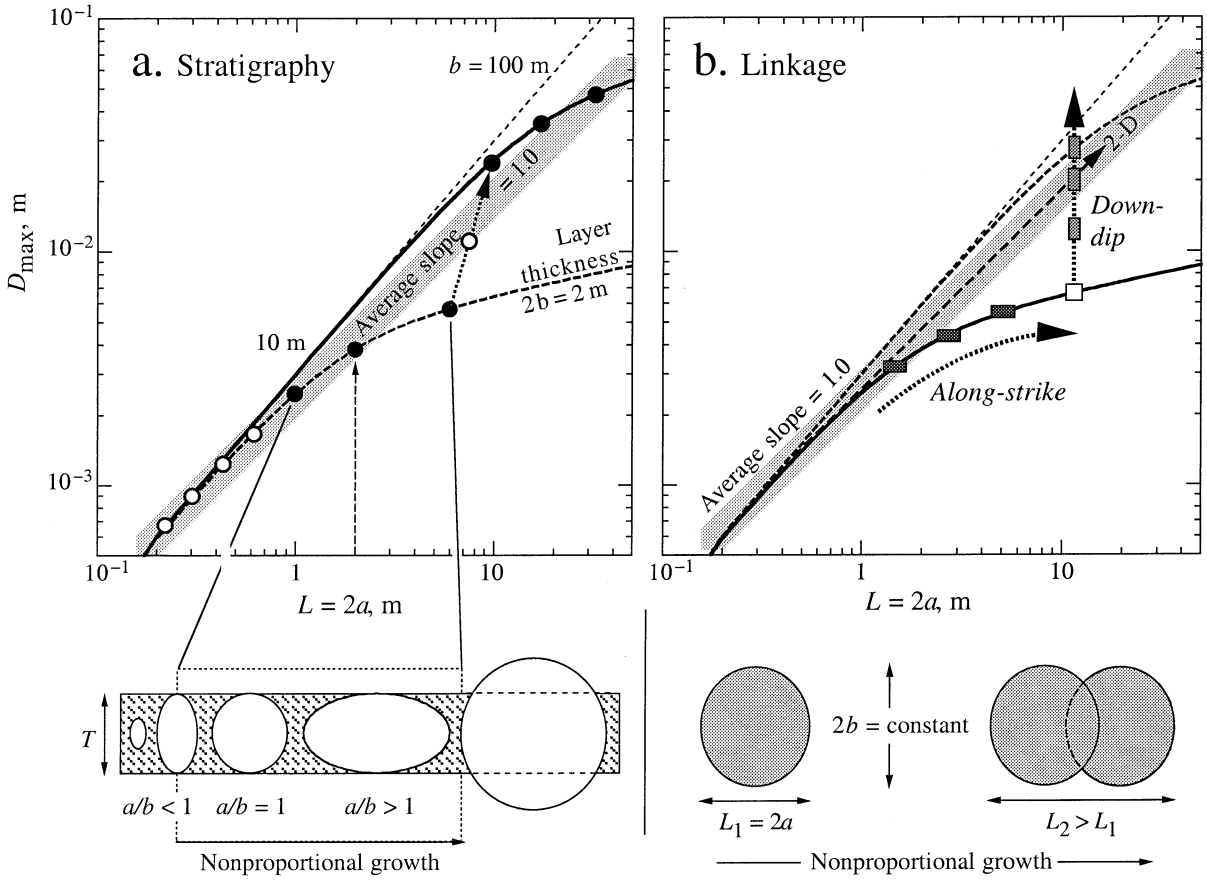

Fig. 19. Displacement–length scaling of fractures that grow faster in one direction (e.g. length) than the other (e.g. height). (a) Confinement of fractures by stratigraphy leads to nonproportional growth (solid symbols) until fracture breaks through bedding and cuts up and/or down section. Fractures may grow nonproportionally again if confined to a thicker layer (upper curve). (b) Fracture linkage produces composite fractures having different aspect ratios than those of the unlinked segments; trajectory on diagram (arrows) depends on the dominant direction of linkage (along-strike vs. down-dip).

6. Discussion and implications

In order for fractures to define a linear scaling relation between maximum displacement and map length, and thereby to define a slope of one on log–log displacement–length diagrams, they must grow in size either two-dimensionally—as 'tall' fractures—or proportionally, either of which implies growth at a constant aspect ratio (Fig. 18a–d). Proportional growth requires that 3-D (elliptical) fractures increase in height as they lengthen. The range of variations in a fracture's aspect ratio contributes a factor of perhaps 5–10 in its displacement values, potentially leading to this degree of scatter on D_{max}/L diagrams (e.g. Willemse et al., 1996; Gudmundsson, 2000). The scatter should be systematic, however, given that increasing fracture aspect ratio is associated with decreasing displacement magnitudes per unit fracture length. This effect is consistent both qualitatively and quantitatively with the shallower slope of D_{max}/L data for deformation bands that are confined within a particular layer (e_1) of the Entrada Sandstone (Fossen and Hesthammer, 1997; Fig. 17).

Confinement of fractures such as deformation bands (e.g. Aydin, 1978b; Davis, 1999), small faults (e.g. Gross, 1995; Gross et al., 1997; Ackermann et al., 2001; Wilkins and Gross, 2002), and joints (e.g. Bahat and Engelder, 1984; Engelder, 1987; Pollard and Aydin, 1988; Helgeson and Aydin, 1991) to discrete stratigraphic layers (e.g. Fig. 4c) or by crustal rheology (e.g. Scholz, 1982; Cowie, 1998) has been well documented in the field and in the literature. This confinement, and associated preferential growth to larger aspect ratios, can occur when the stress and/or lithologic conditions in adjacent stratigraphic layers are unfavorable for propagation of the fracture into those layers (Fig. 18e and f). Assuming a uniform driving stress, the propagation energy (Pollard and Aydin, 1988) along elliptical fractures is greatest along their (smaller) semi-minor axis directions (Irwin, 1962; Kassir and Sih, 1966), leading to steeper displacement gradients and longer end zones in that direction ($2b$) than elsewhere along the periphery. However, propagation of fractures that impinge on stratigraphic contacts between dissimilar layers will be enhanced or impeded depending on the relative material properties and associated stress states (e.g. Pollard and Aydin, 1988; Helgeson and Aydin, 1991). Impeded fault propagation can lead to increased values of displacement, steeper

displacement gradients (Gupta and Scholz, 2000), and, if the stratigraphic thickness along this (2*b*) direction is smaller than that required for the end zone to balance the near-tip stresses, smaller end zones (e.g. Martel and Pollard, 1989). The fracture will be trapped within its layer if these elevated near-tip stresses cannot meet the new yield criteria across the interface (e.g. Cooke and Underwood, 2001), leading to nonproportional growth.

Initially, growth of bands that are sufficiently small to not impinge on layer boundaries may be proportional (Fig. 19a). Trapping of the band within a layer leads to increasing aspect ratio, nonproportional growth, and a shallowing slope on the D_{max}/L diagram (Fig. 19a; Fossen and Hesthammer, 1997, 1998). Once a faulted band breaks through the layer, however, it can follow a steeper trajectory on the D_{max}/L diagram until it becomes confined within a thicker sequence (Fig. 19a). Fossen and Hesthammer (1997) inferred a steeper growth path (e.g. Nicol et al., 1996) that connected deformation bands within the Entrada Sandstone to the larger faulted bands studied by Krantz (1988). We suggest that a decrease in aspect ratio, leading to the steeper growth path (Fig. 19a), was enabled by the nucleation of fault slip surfaces on the bands that facilitated their ability to cut across stratigraphic boundaries.

Linkage of deformation bands, or fractures in general, leads to trajectories on the D_{max}/L diagram analogous to the effect of a confining stratigraphy (Fig. 19b). Because along-strike (horizontal) linkage serves to increase aspect ratio, linked arrays behave as 'longer' elliptical fractures that can accommodate less displacement per unit map length than their 2-D ('tall') counterparts, as recently demonstrated in numerical simulations (Willemse and Pollard, 2000). Fractures and arrays that increase in length *L* by segment linkage must follow a progressively shallowing growth path on the D_{max}/L diagram (Fig. 19b). On the other hand, down-dip (vertical) linkage increases 2*b* instead of 2*a*, leading to a decrease in aspect ratio (to 'taller' fractures) and an increase in the relative amount of displacement accommodated along the aggregate fracture. Down-dip linkage (by itself, with no increase in *L*) would be associated with vertical growth paths on the D_{max}/L diagram (Fig. 19b). These growth paths, defined by the aggregate fracture aspect ratio, provide a physical basis for the 'stair-step' growth sequence proposed by Cartwright et al. (1995). Fracture growth by segment linkage in three dimensions would follow a unit slope if the rates of segment linkage were comparable, on average, in both directions (shaded bar in Fig. 19). Preferential linkage in either direction would lead to displacement discrepancies relative to 2-D expectations and consequent scatter on the D_{max}/L diagram.

7. Conclusions

The magnitude of maximum displacement along a fracture depends on both dimensions of its geometry (length and height) in addition to driving stress and rock mass properties. As a result, relating D_{max} to map length (or down-dip height) alone provides an incomplete assessment of the control of displacement magnitude by this fracture dimension. Although D_{max}/L diagrams relate only two of the three key parameters (D_{max} and *L* but not *H*), the dependence of D_{max} on aspect ratio can be represented, with a small increase in complexity, on these diagrams (Figs. 13 and 14). Because particular mechanisms such as mechanical interaction and linkage affect the aggregate shapes of fractures and fracture arrays in 3-D, scatter on D_{max}/L diagrams can represent variations in fracture aspect ratio.

The deformation bands investigated in this paper are confined to a particular layer within the Entrada Sandstone, and hence have a fixed maximum height. Increases in their map lengths require that their aspect ratios also increase, leading to a systematic reduction in the amount of displacement they can accommodate per unit length and shallower slopes on the D_{max}/L diagram. Formation and growth of deformation bands is sensitive to rock properties, similar to other classes of fractures such as anticracks (compaction seams, stylolites) and dilatant cracks. A nonlinear 3-D displacement–length scaling relation is likely to be associated also with these classes of structures, rather than a linear one on a D_{max}/L diagram, provided their heights remain limited by the layer thickness. Because faults (with well-developed slip surfaces) readily cut across bedding, scaling relations for faults (or faulted deformation bands) are less strongly affected by stratigraphy, leading to fault shapes that produce a unit power-law slope on the D_{max}/L diagram. As a result, standard displacement–length scaling relations (with unit slopes) are most applicable to faults.

The hypotheses presented in this paper can be tested by measuring D_{max}, *a*, and *b* for deformation bands, faulted bands, and other fracture types in relation to the layer thickness. Stratigraphically or rheologically confined fractures that are sufficiently long for their aspect ratios to exceed 5–10 should provide reliable data sets for a 3-D analysis of displacement–length scaling. We anticipate that other fracture types, such as dilatant cracks and stylolites (or compaction seams), should exhibit aspect-ratio scaling if they are mechanically confined to particular beds, leading to progressively larger aspect ratios and, potentially, nonproportional displacement–length scaling.

Acknowledgements

After simmering for some time, this project was launched while the first author was enjoying a pleasant sabbatical leave visit to the University of Bergen in February 1999 and refined during visits to Goblin Valley, Utah, in June 2000 and May 2001. Discussions with Roy Gabrielsen, Agust Gudmundsson, Zoe Shipton, Steve Ahlgren, Atilla Aydin, and Chris Wibberley helped clarify some of the finer points of deformation bands and displacement length

scaling. Scott Wilkins graciously checked the equations. We are grateful for reviews by A. Nicol, Jim Evans, and an anonymous reviewer, and a thorough critique by Steve Martel, that led to substantial improvements in the final version. Thanks to Rick Allmendinger for use of his stereonet program. The work was funded in part by grants from NASA's Planetary Geology and Geophysics Program (to RAS), from the donors of the Petroleum Research Fund, administered by the American Chemical Society (to RAS), and from Statoil (to HF).

References

Ackermann, R.V., Schlische, R.W., Withjack, M.O., 2001. The geometric and statistical evolution of normal fault systems: an experimental study of the effects of mechanical layer thickness on scaling laws. Journal of Structural Geology 23, 1803–1819.

Anderson, T.L., 1995. Fracture Mechanics: Fundamentals and Applications. 2nd Ed. CRC Press, Boca Raton, FL.

Antonellini, M., Aydin, A., 1995. Effect of faulting on fluid flow in porous sandstones: geometry and spatial distribution. American Association of Petroleum Geologists Bulletin 79, 642–671.

Antonellini, M., Pollard, D.D., 1995. Distinct element modeling of deformation bands in sandstone. Journal of Structural Geology 17, 1165–1182.

Antonellini, M., Aydin, A., Pollard, D.D., 1994. Microstructure of deformation bands in porous sandstones at Arches National Park, Utah. Journal of Structural Geology 16, 941–959.

Aydin, A., 1978a. Faulting in sandstone. Ph.D. dissertation, Stanford University.

Aydin, A., 1978b. Small faults formed as deformation bands in sandstone. Pure and Applied Geophysics 116, 913–930.

Aydin, A., Johnson, A., 1978. Development of faults as zones of deformation bands and as slip surfaces in sandstone. Pure and Applied Geophysics 116, 931–942.

Aydin, A., Johnson, A., 1983. Analysis of faulting in porous sandstones. Journal of Structural Geology 5, 19–31.

Bahat, D., Engelder, T., 1984. Surface morphology on cross-fold joints of the Appalachian Plateau, New York and Pennsylvania. Tectonophysics 104, 299–313.

Barenblatt, G.I., 1962. The mathematical theory of equilibrium cracks in brittle fracture. Advances in Applied Mechanics 7, 55–125.

Bésuelle, P., 2001. Compacting and dilating shear bands in porous rock: theoretical and experimental conditions. Journal of Geophysical Research 106, 13,435–13,442.

Beyer, W.H., 1987. CRC Standard Mathematical Tables. 28th EdCRC Press, Boca Raton, FL 674pp.

Bilby, B.A., Cotterell, A.H., Swindon, K.H., 1963. The spread of plastic yield from a notch. Proceedings of the Royal Society of London A272, 304–314.

Boas, M.L., 1966. Mathematical Methods in the Physical Sciences. Wiley, New York 778pp.

Bonnet, E., Bour, O., Odling, N.E., Davy, P., Main, I., Cowie, P., Berkowitz, B., 2001. Scaling of fracture systems in geological media. Reviews of Geophysics 39, 347–383.

Bürgmann, R., Pollard, D.D., Martel, S.J., 1994. Slip distributions on faults: effects of stress gradients, inelastic deformation, heterogeneous host-rock stiffness, and fault interaction. Journal of Structural Geology 16, 1675–1690.

Cartwright, J.A., Mansfield, C.S., 1998. Lateral displacement variation and lateral tip geometry of normal faults in the Canyonlands National Park, Utah. Journal of Structural Geology 20, 3–19.

Cartwright, J.A., Trudgill, B.D., Mansfield, C.S., 1995. Fault growth by segment linkage: an explanation for scatter in maximum displacement and trace length data from the Canyonlands Grabens of SE Utah. Journal of Structural Geology 17, 1319–1326.

Chell, G.G., 1977. The application of post-yield fracture mechanics to penny-shaped and semi-circular cracks. Engineering Fracture Mechanics 9, 55–63.

Cladouhos, T.T., Marrett, R., 1996. Are fault growth and linkage models consistent with power-law distributions of fault lengths? Journal of Structural Geology 18, 281–293.

Clark, R.M., Cox, S.J.D., 1996. A modern regression approach to determining fault displacement–length scaling relationships. Journal of Structural Geology 18, 147–152.

Cooke, M.L., 1997. Fracture localization along faults with spatially varying friction. Journal of Geophysical Research 102, 22,425–22,434.

Cooke, M.L., Underwood, C.A., 2001. Fracture termination and step-over at bedding interfaces due to frictional slip and interface opening. Journal of Structural Geology 23, 223–238.

Cowie, P.A., 1998. Normal fault growth in three-dimensions in continental and oceanic crust. In: Buck, W.R., Delaney, P.T., Karson, J.A., Lagabrielle, Y. (Eds.), Faulting and Magmatism at Mid-Ocean Ridges. American Geophysical Union Geophysical Monograph 106, pp. 325–348.

Cowie, P.A., Scholz, C.H., 1992a. Displacement–length scaling relationship for faults: data synthesis and discussion. Journal of Structural Geology 14, 1149–1156.

Cowie, P.A., Scholz, C.H., 1992b. Physical explanation for the displacement-length relationship of faults using a post-yield fracture mechanics model. Journal of Structural Geology 14, 1133–1148.

Cowie, P.A., Shipton, Z.K., 1998. Fault tip displacement gradients and process zone dimensions. Journal of Structural Geology 20, 983–997.

Crider, J.G., Pollard, D.D., 1998. Fault linkage: three-dimensional mechanical interaction between échelon normal faults. Journal of Geophysical Research 103, 24,373–24,391.

Cruikshank, K.M., Zhao, G., Johnson, A.M., 1991. Duplex structures connecting fault segments in Entrada Sandstone. Journal of Structural Geology 13, 1185–1196.

Das, B.M., 1983. Advanced Soil Mechanics. McGraw-Hill, New York.

Davis, G.H., 1999. Structural geology of the Colorado Plateau region of southern Utah, with special emphasis on deformation bands. Geological Society of America Special Paper 342, 157pp.

Dawers, N.H., Anders, M.H., Scholz, C.H., 1993. Growth of normal faults: displacement–length scaling. Geology 21, 1107–1110.

Du, Y., Aydin, A., 1993. The maximum distortional strain energy density criterion for shear fracture propagation with applications to the growth paths of en échelon faults. Geophysical Research Letters 20, 1091–1094.

Dugdale, D.S., 1960. Yielding of steel sheets containing slits. Journal of the Mechanics and Physics of Solids 8, 100–104.

Engelder, T., 1987. Joints and shear fractures in rock. In: Atkinson, B.K. (Ed.). Fracture Mechanics of Rock. Academic Press, London, pp. 27–69.

Engelder, T., Fischer, M.P., Gross, M.R., 1993. Geological aspects of fracture mechanics. Geological Society of America Short Course Notes, 281 pp.

Fossen, H., 2000. Strukturgeologisk Ekskursjon G-300 Våren 2000 til Coloradoplatået, Unpublished field guide, University of Bergen, Norway (in Norwegian), 37pp.

Fossen, H., Hesthammer, J., 1997. Geometric analysis and scaling relations of deformation bands in porous sandstone. Journal of Structural Geology 19, 1479–1493.

Fossen, H., Hesthammer, J., 1998. Deformation bands and their significance in porous sandstone reservoirs. First Break 16, 21–25.

Goodier, J.N., 1968. Mathematical theory of equilibrium cracks. In: Liebowitz, H. (Ed.). Fracture, Vol. II. Academic Press, New York, pp. 1–66.

Green, A.E., Sneddon, I.N., 1950. The distribution of stresses in the neighborhood of a flat elliptical crack in an elastic solid. Proceedings of the Cambridge Philosophical Society 46, 159–163.

Gross, M.R., 1995. Fracture partitioning: failure mode as a function of lithology in the Monterey Formation of coastal California. Geological Society of America Bulletin 107, 779–792.

Gross, M.R., Gutiérrez-Alonso, G., Bai, T., Wacker, M.A., Collinsworth, K.B., Behl, R.J., 1997. Influence of mechanical stratigraphy and kinematics on fault scaling relationships. Journal of Structural Geology 19, 171–183.

Gudmundsson, A., 2000. Fracture dimensions, displacements and fluid transport. Journal of Structural Geology 22, 1221–1231.

Gudmundsson, A., Bäckström, K., 1991. Structure and development of the Sveeinagja graben, Northeast Iceland. Tectonophysics 200, 111–125.

Gupta, A., Scholz, C.H., 2000. A model of normal fault interaction based on observations and theory. Journal of Structural Geology 22, 865–879.

Heald, P.T., Spink, G.M., Worthington, P.J., 1972. Post yield fracture mechanics. Materials Science and Engineering 10, 129–138.

Helgeson, D.E., Aydin, A., 1991. Characteristics of joint propagation across layer interfaces in sedimentary rocks. Journal of Structural Geology 13, 897–911.

Ingraffea, A.R., 1987. Theory of crack initiation and propagation in rock. In: Atkinson, B.K. (Ed.). Fracture Mechanics of Rock. Academic Press, London, pp. 71–110.

Irwin, G.R., 1962. The crack extension force for a part-through crack in a plate. Journal of Applied Mechanics 29, 651–654.

Issen, K.A., Rudnicki, J.W., 2001. Theory of compaction bands in porous rock. Physics and Chemistry of the Earth (A) 26, 95–100.

Jamison, W.R., 1989. Fault-fracture strain in Wingate Sandstone. Journal of Structural Geology 11, 959–974.

Kanninen, M.F., Popelar, C.H., 1985. Advanced Fracture Mechanics. Oxford University Press, New York.

Kassir, M.K., Sih, G.C., 1966. Three-dimensional stress distribution around an elliptical crack under arbitrary loadings. Journal of Applied Mechanics 33, 601–611.

Kattenhorn, S.A., Aydin, A., Pollard, D.D., 2000. Joints at high angles to normal fault strike: an explanation using 3-D numerical models of fault-perturbed stress fields. Journal of Structural Geology 22, 1–23.

Khazan, Y.M., Fialko, Y.A., 1995. Fracture criteria at the tip of fluid-driven cracks in the Earth. Geophysical Research Letters 22, 2541–2544.

Krantz, R.W., 1988. Multiple fault sets and three-dimensional strain: theory and application. Journal of Structural Geology 10, 225–237.

Lawn, B.R., 1993. Fracture of Brittle Solids. 2nd Ed. Cambridge University Press, New York.

Li, V.C., 1987. Mechanics of shear rupture applied to earthquake zones. In: Atkinson, B.K. (Ed.). Fracture Mechanics of Rock. Academic Press, London, pp. 351–428.

Li, V.C., Liang, E., 1986. Fracture processes in concrete and fiber reinforced cementitious composites. Journal of Engineering Mechanics 112, 566–586.

Mair, K., Main, I., Elphick, S., 2000. Sequential growth of deformation bands in the laboratory. Journal of Structural Geology 22, 25–42.

Martel, S.J., 1997. Effects of cohesive zones on small faults and implications for secondary fracturing and fault trace geometry. Journal of Structural Geology 19, 835–847.

Martel, S.J., Pollard, D.D., 1989. Mechanics of slip and fracture along small faults and simple strike-slip fault zones in granitic rock. Journal of Geophysical Research 94, 9417–9428.

Martel, S.J., Boger, W.A., 1998. Geometry and mechanics of secondary fracturing around small three-dimensional faults in granitic rock. Journal of Geophysical Research 103, 21,299–21,314.

Menéndez, B., Zhu, W., Wong, T.-F., 1996. Micromechanics of brittle faulting and cataclastic flow in Berea sandstone. Journal of Structural Geology 18, 1–16.

Moore, J.M., Schultz, R.A., 1999. Processes of faulting in jointed rocks of Canyonlands National Park, Utah. Geological Society of America Bulletin 111, 808–822.

Muraoka, H., Kamata, H., 1983. Displacement distribution along minor fault traces. Journal of Structural Geology 5, 483–495.

Nicol, A., Watterson, J., Walsh, J.J., Childs, C., 1996. The shapes, major axis orientations and displacement patterns of fault surfaces. Journal of Structural Geology 18, 235–248.

Olson, J.E., 1993. Joint pattern development: effects of subcritical crack growth and mechanical crack interaction. Journal of Geophysical Research 98, 12,251–12,265.

Olsson, W.A., 2000. Origin of Lüders' bands in deformed rock. Journal of Geophysical Research 105, 5931–5938.

Palmer, A.C., Rice, J.R., 1972. The growth of slip surfaces in the progressive failure of over-consolidated clay. Proceedings of the Royal Society of London A332, 527–548.

Paris, P.C., Sih, G.C., 1965. Stress analysis of cracks. In: Fracture Toughness Testing and its Applications. American Society for Testing and Materials, Special Technical Publication 381, pp. 30–83.

Peacock, D.C.P., Sanderson, D.J., 1993. Estimating strain from fault slip using a line sample. Journal of Structural Geology 12, 1513–1516.

Pollard, D.D., Segall, P., 1987. Theoretical displacements and stresses near fractures in rock: with applications to faults, joints, veins, dikes, and solution surfaces. In: Atkinson, B.K. (Ed.). Fracture Mechanics of Rock. Academic Press, London, pp. 277–349.

Pollard, D.D., Aydin, A., 1988. Progress in understanding jointing over the past century. Geological Society of America Bulletin 100, 1181–1204.

Pollard, D.D., Saltzer, S.D., Rubin, A.M., 1993. Stress inversion methods: are they based on faulty assumptions? Journal of Structural Geology 15, 1045–1054.

Priest, S.D., 1993. Discontinuity Analysis for Rock Engineering. Chapman and Hall, New York.

Rekash, V.G., 1979. Manual of the Theory of Elasticity. Mir Publishers, Moscow.

Renshaw, C.E., 1997. Mechanical controls on the spatial density of opening-mode fracture networks. Geology 25, 923–926.

Rubin, A.M., 1992. Dike-induced faulting and graben subsidence in volcanic rift zones. Journal of Geophysical Research 97, 1839–1858.

Rubin, A.M., 1993. Tensile fracture of rock at high confining pressure: implications for dike propagation. Journal of Geophysical Research 98, 15,919–15,935.

Rudnicki, J.W., 1980. Fracture mechanics applied to the Earth's crust. Annual Review of Earth and Planetary Sciences 8, 489–525.

Schlische, R.W., Young, S.S., Ackermann, R.V., Gupta, A., 1996. Geometry and scaling relations of a population of very small rift-related normal faults. Geology 24, 683–686.

Scholz, C.H., 1982. Scaling laws for large earthquakes: consequences for physical models. Seismological Society of America Bulletin 72, 1–14.

Scholz, C.H., 1997. Earthquake and fault populations and the calculation of brittle strain. Geowissenschaften 15, 124–130.

Schultz, R.A., 1999. Understanding the process of faulting: selected challenges and opportunities at the edge of the 21st century. Journal of Structural Geology 21, 985–993.

Schultz, R.A., 2000. Fault-population statistics at the Valles Marineris Extensional Province, Mars: implications for segment linkage, crustal strains, and its geodynamical development. Tectonophysics 316, 169–193.

Segall, P., Pollard, D.D., 1980. Mechanics of discontinuous faults. Journal of Geophysical Research 85, 4337–4350.

Shipton, Z.K., Cowie, P.A., 2001. Damage zone and slip-surface evolution over μm to km scales in high-porosity Navajo sandstone, Utah. Journal of Structural Geology 23, 1825–1844.

Tada, H., Paris, P.C., Irwin, G.R., 2000. The Stress Analysis of Cracks Handbook. 3rd Ed. American Society of Mechanical Engineers, New York.

Timoshenko, S.P., Goodier, J.N., 1970. Theory of Elasticity. 3rd Ed McGraw-Hill, New York 567pp.

Turner, C.E., 1979. Methods for post-yield fracture safety assessment. In: Latzko, D.G.H. (Ed.). Post-Yield Fracture Mechanics. Applied Science Publishers, London, pp. 23–210.

Walsh, J.J., Watterson, J., 1988. Analysis of the relationship between displacements and dimensions of faults. Journal of Structural Geology 10, 239–247.

Watterson, J., 1986. Fault dimensions, displacements and growth. Pure and Applied Geophysics 124, 365–373.

Wibberley, C.A.J., Petit, J.-P., Rives, T., 2000. Mechanics of cataclastic 'deformation band' faulting in high-porosity sandstone, Provence. Earth and Planetary Sciences 331, 419–425 (in French and English).

Wilkins, S.J., Gross, M.R., 2002. Normal fault growth in layered rocks at Split Mountain, Utah: influence of mechanical stratigraphy on dip linkage, fault restriction and fault scaling. Journal of Structural Geology 24, 1413–1429.

Willemse, E.J.M., 1997. Segmented normal faults: correspondence between three-dimensional mechanical models and field data. Journal of Geophysical Research 102, 675–692.

Willemse, E.J.M., Pollard, D.D., 1998. On the orientation and pattern of wing cracks and solution surfaces at the tips of a sliding flaw or fault. Journal of Geophysical Research 103, 2427–2438.

Willemse, E.J.M., Pollard, D.D., 2000. Normal fault growth: evolution of tipline shapes and slip distributions. In: Lehner, F.K., Urai, J.L. (Eds.). Aspects of Tectonic Faulting. Springer, New York, pp. 193–226.

Willemse, E.J.M., Pollard, D.D., Aydin, A., 1996. Three-dimensional analyses of slip distributions on normal fault arrays with consequences for fault scaling. Journal of Structural Geology 18, 295–309.

Wojtal, S.F., 1989. Measuring displacement gradients and strains in faulted rocks. Journal of Structural Geology 11, 669–678.

Xue, Y., Qu, J., 1999. Mixed-mode fracture mechanics parameters of elliptical interface cracks in anisotropic bimaterials. In: Miller, K.J., McDowell, D.L. (Eds.). Mixed-Mode Crack Behavior. ASTM STP 1359. American Society for Testing and Materials, West Conshohocken, PA, pp. 143–159.

Zhu, X.K., Liu, G.T., Chao, Y.J., 2001. Three-dimensional stress and displacement fields near an elliptical crack front. International Journal of Fracture 109, 383–401.